# Dimer Models as Models of Majorana Fermions

Daniel Barron

A report presented upon completion of
the DIAS Summer Studentship Programme.
Supervised by Prof. Denjoe O'Connor.

August 2025

DIAS
Institiúid Ard-Léinn | Dublin Institute for
Bhaile Átha Cliath | Advanced Studies

## Acknowledgements

I would like to thank my supervisor, Prof. Denjoe O'Connor, for his guidance and encouragement throughout this project. Our many discussions over the two months were always helpful, he was willing to answer my questions in detail, and often had a paper to recommend on the topic as well.

I am also grateful to the Dublin Institute for Advanced Studies for the opportunity to undertake this project and for the support provided throughout, and to the programme coordinators, Dr. Dmitry Noshchenko and Dr. Sabine Harribey, for their assistance.

# Abstract

In this report, we investigate the statistical mechanics of dimer models on a variety of two-dimensional lattices, with a particular emphasis on the hexagonal, square–triangle and triangular lattices. By employing Kasteleyn's method, we obtain expressions for the partition function. We explore the universality of critical behaviour by relating these models to the conformal field theory of the Ising model and its Majorana fermion formulation. Different lattices are related through the inclusion of additional bond types, revealing the connection between different lattice geometries through changes in the modular parameter. Exact analytical expressions were plotted, using numerical integration for the final integral, to analyse thermodynamic quantities such as the free energy, internal energy, and specific heat, with a focus on the nature of divergences at the critical points. We also discuss physical interpretations in terms of fermionic field theories, topological defects, and geometric aspects of the underlying lattices.

# Contents

**1 Introduction** **5**

**2 Background** **5**

2.1 Dimer Models and Kasteleyn Theory . . . . . 5

2.1.1 Domino Tilings on a Chessboard . . . . . 7

2.1.2 Melting Corners and Limit Shapes in Dimer Models . . . . . 8

2.1.3 Dimers on Random Causal Triangulations . . . . . 9

2.2 Majorana Fermions and Grassmann Variables . . . . . 9

2.2.1 Majorana Chains and Non-Invertible Symmetries . . . . . 10

**3 The Hexagonal Lattice** **11**

**4 The Square-Triangle Lattice** **16**

**5 The Triangular Lattice** **22**

**6 A Bipartite Hexagonal Lattice with a Defect** **27**

6.1 Case 1: Rectangular Domain . . . . . 28

6.2 Case 2: Equal weights . . . . . 28

6.3 Case 3: At the edge of the Amoeba . . . . . 29

**7 Conclusion** **29**

# 1 Introduction

The study of dimer models occupies a central position in statistical mechanics, both as exactly solvable systems and as a bridge between discrete lattice models and continuum quantum field theories. In a dimer covering (or perfect matching) of a graph, each vertex is incident to exactly one edge, representing a tightly bound pair of particles or spins. These models have attracted sustained interest since Kasteleyn's pioneering solution for planar graphs, owing to their rich combinatorial structure, deep connections to the Ising model, and their role as discrete realizations of free fermion theories.

From the perspective of condensed matter physics, dimer models provide an exactly solvable laboratory for understanding universality, critical phenomena, and the emergence of continuum field theories from lattice systems. In particular, bipartite dimer models are known to correspond to the massless Dirac fermion in the continuum limit, while non-bipartite models map instead to the Majorana fermion and the conformal field theory of the two-dimensional Ising model. The language of Grassmann variables and Pfaffians offers a natural fermionic formulation, in which the partition function is expressed as a weighted sum of Pfaffians of Kasteleyn matrices associated with the lattice.

A further motivation for studying these models is their modular and topological structure when placed on higher-genus surfaces, where the enumeration of dimer coverings is intimately related to the classification of spin structures. In such settings, the dependence of the continuum theory on the underlying lattice geometry can be largely encoded in the modular parameter $\tau$, highlighting the universality of the critical behaviour: microscopic differences between similar lattices manifest through the value of $\tau$ at criticality. This observation mirrors the general arguments given in [1], where modular invariance is used to connect lattice discretisations to continuum CFT data. However, there is also special behaviour exhibited by the model for certain values of the bond activities, such as mod 6 or mod 8 holonomies. There is also potential for more general holonomies depending on the exact values of the weights.

In this work, we investigate both bipartite and non-bipartite dimer models, focusing on the hexagonal, square–triangle, and triangular lattices. By explicitly computing free energies, internal energies, and specific heats, both numerically and analytically, we explore their singular behaviour near the critical point. The connection between lattice dimers, fermionic field theories, and conformal field theory is made explicit, and we highlight how changes in lattice structure alter the modular parameter, as well as how defects on different lattices can lead to non-trivial consequences for the partition function and therefore the thermodynamic properties of those lattices.

# 2 Background

## 2.1 Dimer Models and Kasteleyn Theory

A *dimer covering* of a graph $\Gamma$ is a subset of edges such that each vertex in the graph is incident to exactly one edge in the subset [2]. In other words, every vertex is matched with one neighbour, and no two dimers share a vertex. Such configurations are also referred to as *perfect matchings*. Fig. 1 is a simple example of the two dimer coverings of a $2 \times 2$ square graph.



Figure 1: *Two dimer coverings of a* $2 \times 2$ *square graph.*

In a physical interpretation, the edges may represent bonds between particles, each assigned an energy $\epsilon_e$. The total energy of a dimer configuration $D$ is then given by

$$E(D) = \sum_{e \in D} \epsilon_e. \tag{1}$$

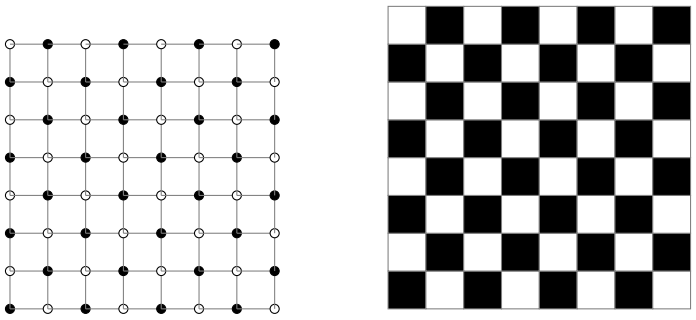
The probability of observing a given configuration $D$ at inverse temperature $\beta$ follows Boltzmann statistics:

$$\Pr(D) = \frac{e^{-\beta E(D)}}{\mathcal{Z}}, \quad \text{where} \quad \mathcal{Z} = \sum_{\text{all } D} e^{-\beta E(D)} \text{ is the canonical partition function.} \tag{2}$$

The partition function can also be written as a product over the occupied bond activities $a_i$ on bond type $i$ to the power of the number of occurrences of that bond activity $N_i$:

$$\mathcal{Z} = \sum_{\text{all } D} \prod_i a_i^{N_i} \tag{3}$$

In practice, one often studies dimer models on planar graphs, where powerful combinatorial tools apply. A key notion is the *dual graph* $\Gamma'$, constructed by placing a vertex inside each face of $\Gamma$ and drawing edges between dual vertices that cross an edge of $\Gamma$. There is a one-to-one correspondence between dimer coverings on $\Gamma$ and certain tilings on $\Gamma'$. In the case of bipartite graphs, where vertices are divided into two sets (e.g., black and white) such that no two vertices of the same set are adjacent, the dual graph exhibits a chessboard-like pattern. A classic example is the $8 \times 8$ square lattice, whose dual graph is a chessboard.



Bipartite Square Grid Graph  Dual Graph: Chessboard

Figure 2: *A bipartite square grid graph and its dual graph.*

To compute the partition function, one may use a technique pioneered by Kasteleyn. The key is to assign an orientation to each edge of the planar graph $\Gamma$ so that each face of the graph has an odd number of edges oriented clockwise. This is known as a *Kasteleyn orientation*. Given such an orientation and a set of edge weights, one constructs what is known as a Kasteleyn matrix $K$, whose entries are signed weights of the edges. For an edge $e$ pointing from a vertex $i$ to a vertex $j$, $K_{ij} = e^{-\beta\epsilon_e}$ and $K_{ji} = -e^{-\beta\epsilon_e}$, i.e. $K$ is an anti-symmetric matrix. For bipartite graphs with $2n$ vertices, one can number black vertices by the first $n$ indices, and white vertices by the second $n$ indices. In this case, $K$ takes the form:

$$K = \begin{pmatrix} 0 & A \\ -A^T & 0 \end{pmatrix}, \tag{4}$$

where $A$ is an $n \times n$ matrix mapping from black to white vertices. The sign of each entry depends on the orientation: if the edge is directed from a black to a white vertex, the sign is $+1$, otherwise $-1$.

Kasteleyn showed that the partition function is given by the Pfaffian of $K$ [3]:

$$\mathcal{Z}(\Gamma) = |\text{Pf}(K)|, \tag{5}$$

Note since the energies are real the coefficients of $K$ are real, then $\text{Pf}(K)^2 = |\det(K)|$. It is possible $|\det(K)|$ is negative, but the square of a real number must be positive. For graphs embedded on closed oriented surfaces of genus $g$, such as the torus, the full partition function is obtained by summing Pfaffians over $2^{2g}$ distinct Kasteleyn matrices, corresponding to different boundary conditions [4]. Periodic or anti-periodic boundary conditions around the nontrivial cycles of a genus-$g$ surface are called spin structures. Using the same notation as in [5], the partition function is given by:

$$\mathcal{Z}(\Gamma) = \frac{1}{2^g} \sum_{\vec{u} \in S(\Sigma)} \text{Arf}(\vec{u}) \text{Pf}(K_{\vec{u}}), \tag{6}$$

where $\text{Arf}(\vec{u}) = \pm 1$ is the Arf invariant [6] and $K_{\vec{u}}$ is the Kasteleyn matrix with twist $\vec{u}$. For periodic boundary conditions a cycle, $u_i = 0$, whereas for anti-periodic boundary conditions $u_i = \frac{1}{2}$. For instance, for the torus we will consider later in this report, the partition function is given by

$$\mathcal{Z} = (-)^{NM(NM-1)/2} \frac{1}{2} \sum_{u,v=0}^{1/2} e^{2\pi i(1/2+u+v+2uv)} \text{Pf}(K_{\vec{u}}), \tag{7}$$

where $u$ and $v$ represent the boundary conditions for the $x$ and $y$ directions, respectively. In the bipartite case, where $K$ takes the form of Eq. (4), this can be further reduced to:

$$\mathcal{Z} = \frac{1}{2} \sum_{u,v=0}^{1/2} e^{2\pi i(1/2+u+v+2uv)} \det(A_{\vec{u}})$$

This powerful correspondence between dimer models and Pfaffians allows the exact computation of partition functions, correlation functions, and the exploration of topological features such as vortices and spin structures within a unified algebraic framework.

### 2.1.1 Domino Tilings on a Chessboard

The machinery developed by Kasteleyn can be used to answer interesting mathematical questions also, such as the number of domino tilings on a chessboard.

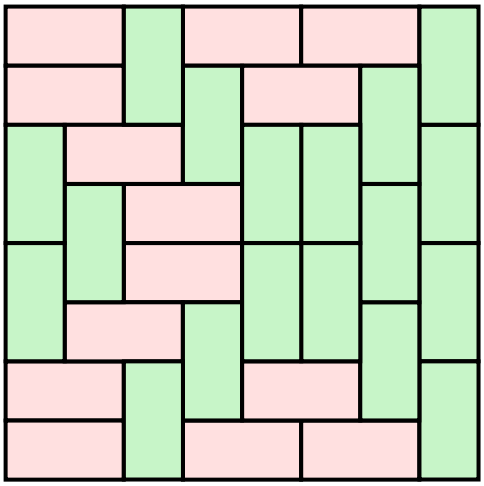


Figure 3: *A domino tiling of an* $8 \times 8$ *square* [7].

This question is fairly easily answered for $2 \times 2$ chessboard, as it is simply the dual of the case considered in Fig. 1.

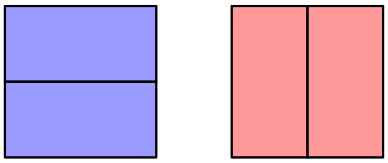


Figure 4: *Domino tilings on a* $2 \times 2$ *square.*

This question becomes considerably more complicated for higher $n \times n$ chessboards however, which is why we use a specific case of Kasteleyn's Theorem. At $\beta = 0$, all bond activities become 1, so

$$\mathcal{Z}|_{\beta=0} = \sum_{\text{coverings}} 1 = \#\{\text{dimer coverings of the graph}\}. \tag{8}$$

One can use this to compute the number of domino tilings on an $n \times n$ chessboard, of which the first few values are given in Table 1.

| Size of board | No. of coverings |
|---|---|
| $2 \times 2$ | 2 |
| $4 \times 4$ | 36 |
| $6 \times 6$ | 6,728 |
| $8 \times 8$ | 12,988,816 |
| $10 \times 10$ | 258,584,046,368 |

Table 1: *Number of domino tilings on an $n \times n$ chessboard.*

In general, the number of domino tilings on an $M \times N$ rectangle [8] is given by:

$$\prod_{j=1}^{\lceil M/2 \rceil} \prod_{k=1}^{\lceil N/2 \rceil} \left[ 4\cos^2\left(\frac{\pi j}{M+1}\right) + 4\cos^2\left(\frac{\pi k}{N+1}\right) \right] \tag{9}$$

### 2.1.2 Melting Corners and Limit Shapes in Dimer Models

Beyond their exact solvability and connections to free fermions, dimer models provide a rich setting for studying emergent large-scale structures in statistical mechanics. A celebrated example is the melting corner problem, which describes the statistical shape of an interface between ordered and disordered regions in certain tiling models.

In the context of lozenge tilings (which are equivalent to close-packed dimers on the hexagonal lattice), the melting corner setup corresponds to removing a large quadrant from a fully packed tiling and allowing the system to fluctuate thermally. Microscopically, the configurations are random tilings, but macroscopically, a limit shape emerges in the thermodynamic limit: a deterministic boundary separates the frozen ordered regions from the temperate disordered region.

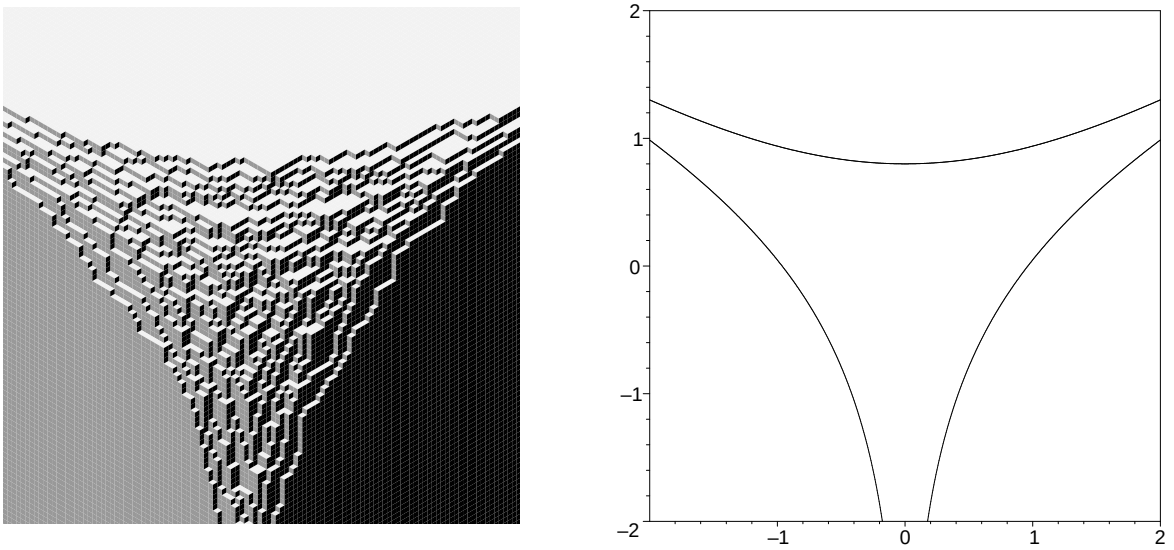



Figure 5: *On the left is the height function of a random volume-constrained dimer configuration on the honeycomb lattice. The boundary conditions here are that of a crystal corner: all dimers are aligned the same way deep enough in each of the 3 sectors. On the right is the amoeba of a straight line [9].*

This melting corner picture has deep connections to enumerative combinatorics, representation theory, and even crystal melting, where the height function of the dimer model encodes a stepped surface receding from a corner.

### 2.1.3 Dimers on Random Causal Triangulations

In their work, Ambjørn, Durhuus, and Wheater [10] investigate a model of hard dimers placed on two-dimensional random causal triangulations (CDTs), a class of discrete quantum gravity models characterized by a well-defined notion of causal structure. The motivation is to understand the effect of matter degrees of freedom—represented here by dimers—on the geometry of spacetime at the discrete level.

A CDT is constructed by gluing together triangles in a way that respects a global foliation into spatial slices labeled by discrete time steps. The triangulations are rooted and constructed in a planar fashion, resulting in a tree-like causal structure. The authors consider a restricted dimer model in which dimers can only occupy a specific subset of the edges: namely, the vertical edges connecting time slices, subject to the constraint that each edge can be covered by at most one dimer and no vertex is incident to more than one dimer.

This setup defines a coupled statistical system of random geometries and matter fields. The key observable is the partition function $Z(\mu, \xi)$, which counts triangulations weighted by a chemical potential $\mu$ (controlling the cosmological constant) and a dimer activity $\xi$. The model exhibits a rich phase structure, including a critical point beyond which the average geometry becomes non-compact. By solving recursion relations for generating functions, the authors derive exact expressions for critical lines and exponents characterizing the continuum limit.

Importantly, the presence of dimers modifies the universality class of the model. Unlike pure CDT, which belongs to the universality class of branched polymers, the dimer-decorated model exhibits nontrivial scaling behavior. The critical exponent associated with the string susceptibility differs from the pure gravity case, indicating that even a restricted set of matter configurations can back-react on the underlying geometry in a meaningful way.

This work provides one of the first exactly solvable models of matter-coupled CDT and serves as a foundation for further studies of statistical systems and quantum fields on random discrete geometries. The restriction to a solvable dimer ensemble allows the authors to isolate geometric effects in a controlled way, offering insight into the interplay between combinatorics and quantum geometry.

## 2.2 Majorana Fermions and Grassmann Variables

Grassman variables are elements of basis vectors of a vector space, which form an unital algebra over a field [11]. These generators obey the following relations [12]:

$$\begin{aligned} \chi_i\chi_j = -\chi_j\chi_i \implies \chi_i^2 = 0 \\ \int d\chi_i = 0, \quad \int \chi_i \, d\chi_i = 1 \end{aligned} \tag{10}$$

These properties are the foundation of Grassmann integration (Berezin integration), which plays a central role in the fermionic formulation of the dimer model. For a $2 \times 1$ fundamental tile hexagonal lattice, which will be explained in more detail later in the report, the Kasteleyn matrix for is given by:

$$K = \begin{pmatrix} 0 & 0 & c-b & -a \\ 0 & 0 & -a & c-b \\ b-c & a & 0 & 0 \\ a & b-c & 0 & 0 \end{pmatrix}, \quad \mathrm{Pf}(K) = (c-b)^2 - a^2 \tag{11}$$

Now we will compute the Grassmanian Gaussian or Berezin integral for this, giving each lattice point a Grassmannian variable $\chi_i$.

$$\begin{aligned} I &= \int [d\chi] e^{-\frac{1}{2}\sum_{i,j}\chi_i K_{ij}\chi_j} \\ &= \int [d\chi] \prod_{i,j} \left(1 - \frac{1}{2}\chi_i K_{ij}\chi_j\right) \\ &= \frac{1}{4}\int [d\chi] \left(\chi_1\chi_3 \left(K_{13} - K_{31}\right)\chi_2\chi_4 \left(K_{24} - K_{42}\right) + \chi_1\chi_4(K_{14} - K_{41})\chi_2\chi_3(K_{23} - K_{32})\right) \\ &= (c-b)^2 - a^2 = \mathrm{Pf}(K) \end{aligned} \tag{12}$$

This demonstrates explicitly that the Berezin integral yields the Pfaffian of the Kasteleyn matrix. Many things point towards the equivalence of the dimer model and the free fermion on the same lattice in the continuum limit. The dimer model is known to correspond to the two-dimensional Ising model, as will be shown later in the report. In the continuum limit, the Ising model near the critical point corresponds to the free Majorana fermion. In addition to this, the one-to-one correspondance between the $2^{2g}$ Kasteleyn matrices mentioned earlier and the different spin structures was proved in [4]. In [13] it was shown that the dimer model on a square lattice can be naturally mapped to the dynamics of a free massless fermion on the same lattice. Starting by associating a two component real spinor $\psi = (\chi_\bullet, \chi_\circ)$ to each pair of black and white vertices of the bipartite graph, the continuum free massless fermion action is

$$S = \int d^2x \; \bar{\psi}(x) \, \partial\!\!\!/ \, \psi(x), \tag{13}$$

with $\partial\!\!\!/ = \gamma^\mu \partial_\mu$, where $\gamma^\mu$ are Pauli matrices which satisfy the Clifford algebra $\{\gamma^\mu, \gamma^\nu\} = 2\delta^{\mu\nu}$. On the lattice, the derivative $\partial_\mu$ is replaced by the symmetric finite difference

$$\partial_\mu \quad \longrightarrow \quad \frac{\exp(a^\mu \partial_\mu) - \exp(-a^\mu \partial_\mu)}{2|a^\mu|}, \tag{14}$$

where the $a^\mu$ are lattice vectors connecting nearest neighbours. The minus sign in the action under interchange of $\psi$ variables follows naturally from their Grassmann nature. This gives the discrete Dirac operator $\partial\!\!\!/(x, y)$, which for a square lattice has the block structure

$$\begin{aligned} S &= \sum_{\langle x,y \rangle} \chi(x) \, \partial\!\!\!/(x,y) \, \chi(y), \\ \partial\!\!\!/(x,y) &= \gamma^\mu \frac{x_\mu - y_\mu}{|x-y|}. \end{aligned} \tag{15}$$

For a bipartite graph, again labelling black sites $\bullet$ and white sites $\circ$, the action becomes

$$S = \begin{pmatrix} \tilde{\chi}_\bullet & \tilde{\chi}_\circ \end{pmatrix} \begin{pmatrix} 0 & \partial\!\!\!/_{\bullet\circ} \\ \partial\!\!\!/_{\circ\bullet} & 0 \end{pmatrix} \begin{pmatrix} \tilde{\chi}_\bullet \\ \tilde{\chi}_\circ \end{pmatrix} = \tilde{\chi}_\bullet \cdot \partial\!\!\!/_{\bullet\circ} \cdot \tilde{\chi}_\circ + \tilde{\chi}_\circ \cdot \partial\!\!\!/_{\circ\bullet} \cdot \tilde{\chi}_\bullet, \tag{16}$$

which is Eq. (14) of [13]. The operator $\partial\!\!\!/_{\bullet\circ}$ is non-zero only for nearest neighbours, and its entries are proportional to the components of the $\gamma^\mu$. Choosing

$$\gamma^1 = \begin{pmatrix} 0 & 1 \\ 1 & 0 \end{pmatrix}, \quad \gamma^2 = \begin{pmatrix} 0 & i \\ -i & 0 \end{pmatrix}, \tag{17}$$

the link weights become $\{1, \, i, \, -1, \, -i\}$ around each black vertex, giving precisely a Kasteleyn orientation. In the bipartite case, the discretised Dirac operator reduces to the Kasteleyn matrix $K$. The fermionic partition function then becomes

$$\mathcal{Z}_{\text{fermion}} = \int [d\psi] \, e^{-S[\psi]} = \sqrt{\det(\partial\!\!\!/)} = \sqrt{\det K} = \text{Pf}(K), \tag{18}$$

where the phase of the square root must be chosen consistently. This equality makes the connection between the fermionic and dimer formulations explicit.

### 2.2.1 Majorana Chains and Non-Invertible Symmetries

The recent work of Seiberg and Shao [14] revisits the 1+1 dimensional Majorana chain, emphasizing how discrete symmetries on the lattice can give rise to rich structures in the continuum limit—including non-invertible symmetries. In this setting, the Hilbert space is built from real fermion operators $\chi_\ell$, defined on sites of a one-dimensional periodic lattice. The model exhibits several discrete symmetries: *lattice translation*, *fermion parity*, *spatial parity*, and *time reversal*, which, crucially, may not always commute in the expected way due to projective realizations and *'t Hooft anomalies*.

A central insight of the paper is that lattice symmetries can emanate into internal symmetries in the Majorana conformal field theory—a phenomenon captured by the notion of *emanant symmetries*[1]. For

[1]The term *emanant symmetry* refers to an internal symmetry in the infrared field theory that descends from a symmetry of the underlying lattice model. Unlike emergent symmetries, which arise accidentally at low energies, emanant symmetries are present in the UV theory and persist into the IR, though they may act in a non-obvious or "non-local" fashion in the continuum description. In this sense, they "emanate" from the microscopic (lattice) symmetries into internal symmetries of the IR field theory.

example, the lattice translation operator in the Majorana chain becomes, in the low-energy continuum limit, the *chiral fermion parity operator* $(-1)^{F_L}$ of the continuum CFT. The algebra of these symmetries reveals an anomaly classified by the group $\mathbb{Z}_8$, a well-known feature of 1+1d fermionic systems.

Through a *Jordan–Wigner transformation*, the Majorana chain maps to the transverse-field Ising model, and summing over spin structures (i.e., performing a *GSO projection*) produces a bosonic theory. Remarkably, this mapping induces a *non-invertible symmetry* when a defect is introduced to the model. The lattice translation symmetry of the fermionic theory becomes a *non-invertible Kramers–Wannier duality operator* in the critical Ising model, obeying fusion rules of the form:

$$D^2 = \tfrac{1}{2}(1+\eta)T_{\text{Ising}}, \tag{19}$$

where $D$ is the non-invertible duality operator, $\eta$ is the spin-flip symmetry, and $T_{\text{Ising}}$ is the Ising lattice translation operator. These fusion rules reflect categorical constraints that go beyond conventional group symmetries and signal the presence of *non-invertible emanant symmetries*.

This construction provides a concrete lattice realization of emergent, non-invertible symmetries in statistical models and highlights the role of Majorana fermions in mediating between microscopic lattice descriptions and their rich continuum limits.

It is worth noting that the Ising model itself admits a reformulation as a dimer model on a suitably chosen (non-bipartite) lattice, which will be discussed later in the report. In this setting, the GSO projection—which in the Majorana chain corresponds to a sum over spin structures—has a precise analogue: it arises naturally in the Kasteleyn formulation of the dimer model on higher-genus surfaces. There, different spin structures correspond to different choices of boundary conditions as mentioned earlier, and summing over them implements the projection to the bosonic theory in Eq. (2). Note Eq. (2) is clearly bosonic as each energy is represented as a product of real positive weights (for the hexagonal lattice, one gets a $a^{N_a}, b^{N_b}, c^{N_c}$ with $N_i$ the number of dimers of type $i$). This procedure can be interpreted as summing (sometimes called integrating in path integral formulations) over a discrete $\mathbb{Z}_2$ gauge field. Thus, the duality between fermionic and bosonic theories, and the emergence of non-invertible symmetries, finds a parallel in the world of dimers.

# 3 The Hexagonal Lattice

To start, we aim to reproduce some results found by Nash and O'Connor for dimers on the periodic hexagonal lattice [15]. For the simplest case of the hexagonal lattice, there are three different types of bonds, denoted by activities $a$, $b$ and $c$. These are shown in the diagram below of a fundamental tile of this lattice, the same type of one used in the Kitaev model [16].

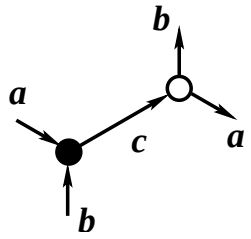



Figure 6: *Fundamental tile of the hexagonal lattice, showing activities of the different bonds and our choice of Kasteleyn orientation.*

Note also that the arrows here denote a Kasteleyn orientation on the edges of the graph. Since this is a bipartite lattice, the Kasteleyn matrix can be written in the same form as in Eq. (4). We can attempt to write down the matrix $A$ for a simple $2 \times 2$ doubly periodic case, using four indices instead of two. These indices as $k_1$, $k_2$, $l_1$ and $l_2$. Here, $(k_1, l_1)$ are the coordinates of the black vertices and $(k_2, l_2)$ are the coordinates of the white vertices. In our coordinate system, $k_1$ and $k_2$ can be thought of as $x$-coordinates, while $l_1$ and $l_2$ can be related to $y$-coordinates, where $(1,1)$ is the bottom left corner tile of the lattice we are looking at and $(N, M)$ is the tile in the top right corner. It should also be noted that $k_1$ and $k_2$ are defined modulo $N$, while $l_1$ and $l_2$ are defined modulo $M$. Now, instead of going from $1, 2 \ldots NM$, the columns and rows of $A$ will now be numbered as $(1,1), (1,2), \ldots, (1,M), (2,1), \ldots, (N,M)$. Our

convention is that the rows are numbered by the black coordinates $(k_1, l_1)$ and the columns by the white coordinates $(k_2, l_2)$.

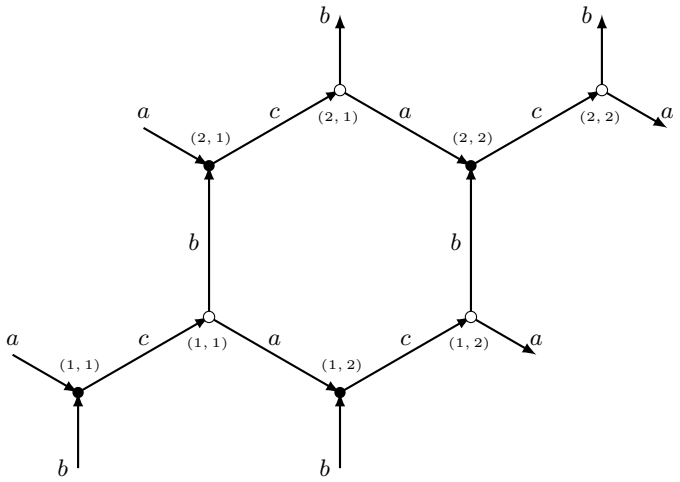



Figure 7: *Small example of our bipartite hexagonal lattice, showing activities of the different bonds and our choice of Kasteleyn orientation.*

The double index $(k, l)$ can be mapped to a single index $i = k + N(l-1)$, so the vertices are labeled from 1 to NM in the matrices $A_{ij}$ and more generally $K_{ij}$. Now, by looking at the graph in Fig. 7, we can build our Kasteleyn matrix for this lattice.

$$A = \begin{pmatrix} c & -a & -b & 0 \\ -a & c & 0 & -b \\ -b & 0 & c & -a \\ 0 & -b & -a & c \end{pmatrix} \tag{20}$$

As mentioned previously, the different terms in Eq. (6) correspond to periodic and anti-periodic boundary conditions in both directions on the lattice. The special form of the Kasteleyn matrix also reduces the Pfaffian of $K$ to a determinant of $A$. Hence, the explicit form of Eq. (6) in this case is given by the following:

$$\mathcal{Z} = \frac{1}{2}\Bigg( - \det \begin{pmatrix} c & -a & -b & 0 \\ -a & c & 0 & -b \\ -b & 0 & c & -a \\ 0 & -b & -a & c \end{pmatrix} + \det \begin{pmatrix} c & a & -b & 0 \\ -a & c & 0 & -b \\ -b & 0 & c & a \\ 0 & -b & -a & c \end{pmatrix} + \dots \tag{21}$$

$$\dots + \det \begin{pmatrix} c & -a & b & 0 \\ -a & c & 0 & b \\ -b & 0 & c & -a \\ 0 & -b & -a & c \end{pmatrix} + \det \begin{pmatrix} c & a & b & 0 \\ -a & c & 0 & b \\ -b & 0 & c & a \\ 0 & -b & -a & c \end{pmatrix} \Bigg) \tag{22}$$

$$= a^4 + b^4 + c^4 + 2a^2b^2 + 2a^2c^2 + 2b^2c^2 = (a^2 + b^2 + c^2)^2 \tag{23}$$

This matches the partition function that one would get from manually drawing these configurations, which are shown in Fig. 8. In general, the doubly periodic $A$ matrix can be written in the form:

$$A_{k_1,k_2;l_1l_2} = c\delta_{k_1,k_2}\delta_{l_1,l_2} - a\delta_{k_1,k_2+1}\delta_{l_1,l_2} - b\delta_{k_1k_2}\delta_{l_1,l_2+1} \tag{24}$$

This matrix can be diagonalised using the eigenvectors $z^k w^{-l}$, one can see

$$A_{k_1,k_2;l_1l_2} z^{k_2} w^{-l_2} = (c - a/z - bw) z^{k_1} w^{-l_1} \tag{25}$$

hence, the eigenvalues are given by what is known as the spectral polynomial,

$$p^{Hex}(z, w) = c - a/z - bw. \tag{26}$$

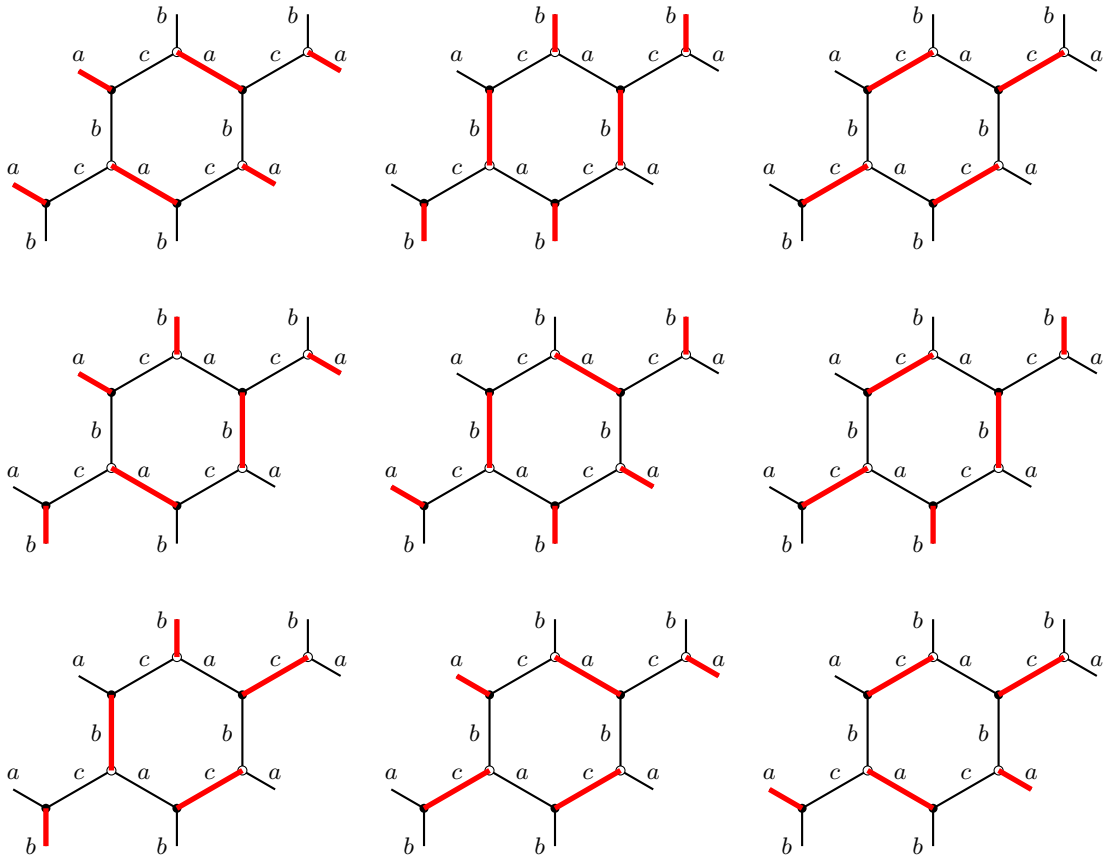



Figure 8: *All configurations for* $2 \times 2$ *fundamental tiles on the hexagonal lattice.*

Now, using the fact that these indices are periodic like the lattice, $z^N = 1$ and $w^M = 1$. Hence, these can be written as simply

$$z = e^{2\pi i n/N} = e^{i\theta_n}, \quad w = e^{2\pi i m/M} = e^{i\phi_m}, \tag{27}$$

where $\theta_n = \frac{2\pi n}{N}$ and $\phi_m = \frac{2\pi m}{M}$[2]. The determinant of $A$ is now just a product over the spectral polynomials:

$$\det(A) = \prod_{n,m=1}^{N,M} \left( c - ae^{-2\pi i n/N} - be^{2\pi i m/M} \right) \tag{28}$$

The zeros of the spectral polynomial in terms of continuum angles are denoted $(\Theta, \Phi)$ and are special points. For any finite $N$ and $M$ the polynomial may only have an approximate zero at the nearest integer to these points but become zeros in the limit of $N$ and $M$ being infinite. To find these special points, one starts with the imaginary part of the equation:

$$a \sin\Theta - b \sin\Phi = 0 \implies \sin\Phi = \frac{a}{b} \sin\Theta \tag{29}$$

[2]From here on in this section, these angles will simply be denoted by $\theta$ and $\phi$ as we take the continuum limit.

Now this can be used with the real part of the spectral polynomial to solve for these angles.

$$\begin{aligned}
&c - a\cos\Theta - b\cos\Phi = 0 \\
\implies &c \pm a\sqrt{1-\sin^2\Theta} \pm b\sqrt{1-\sin^2\Phi} = 0 \\
\implies &c \pm a\sqrt{1-\sin^2\Theta} \pm b\sqrt{1-\left(\frac{a}{b}\right)^2\sin^2\Theta} = 0 \\
\implies &c^2 \pm 2ac\sqrt{1-\sin^2\Theta} + a^2(1-\sin^2\Theta) = b^2\left(1-\left(\frac{a}{b}\right)^2\sin^2\Theta\right) \\
\implies &(c^2+a^2-b^2)^2 = 4a^2c^2(1-\sin^2\Theta) \\
\implies &4a^2c^2\sin^2\Theta = 4a^2c^2 - (c^2+a^2-b^2)^2 = (2ac+c^2+a^2-b^2)(2ac-c^2-a^2-b^2) \\
&= -((a+c)^2-b^2)((a-c)^2-b^2) = (a+b+c)(-a+b+c)(a-b+c)(a+b-c) \\
\implies &\sin\Theta = \frac{b}{2r} \text{ and } \sin\Phi = \frac{a}{2r} \text{ where } r = \frac{abc}{\sqrt{(a+b+c)(-a+b+c)(a-b+c)(a+b-c)}}
\end{aligned} \tag{30}$$

Notice either the positive value of the sines of these angles could have been taken, so there are two solutions to this polynomial, $(\Theta, \Phi)$ and $(-\Theta, -\Phi)$. These can be used to help compute the "Free energy per dimer" $W = \frac{\ln Z}{NM}$. In the thermodynamic limit, the partition function is equivalent to Eq. (28). We can also use the thermodynamic limit to turn what would be a sum into an integral.

$$\begin{aligned}
W &= \frac{1}{NM}\sum_{n,m=1}^{N,M} \ln(c - ae^{-2\pi in/N} - be^{2\pi im/M}) \\
&\approxeq \frac{1}{NM}\iint dndm \ln(c - ae^{-2\pi in/N} - be^{2\pi im/M}) \\
&= \oiint \frac{d\theta d\phi}{4\pi^2}\ln(c - ae^{-i\theta} - be^{i\phi}) \\
&= \ln c + \oiint \frac{d\theta d\phi}{4\pi^2}\ln\left(1 - \frac{a}{c}e^{-i\theta} - \frac{b}{c}e^{i\phi}\right)
\end{aligned} \tag{31}$$

To reproduce the result of Eq. (9) in [15], we now wish to compute the $\phi$ integral using the identity:

$$\oint d\phi \ln\left(K - \frac{b}{c}e^{i\phi}\right) = 2\pi\ln\left(\max\left(|K|, \left|\frac{b}{c}\right|\right)\right) \tag{32}$$

In this case $K(\theta) = 1 - \frac{a}{c}e^{-i\theta}$, so one needs to find the region in $\theta$ for which $|K(\theta)| > \left|\frac{b}{c}\right|$, and the region for which $|K(\theta)| < \left|\frac{b}{c}\right|$. These magnitudes must be equal at the angles $\pm\Theta$ defined above, so one can see at which angle $|K(\theta)|^2$ is increasing or decreasing.

$$\begin{aligned}
|K(\theta)|^2 &= 1 + \frac{a^2}{c^2} - \frac{2a}{c}\cos\theta \\
\frac{d}{d\theta}|K(\theta)|^2 &= \frac{2a}{c}\sin\theta \implies |K(\theta)| \text{ is } \begin{cases}\text{decreasing at } \theta = -\Theta \\ \text{increasing at } \theta = \Theta\end{cases}
\end{aligned} \tag{33}$$

Now we can use this to say that in the following intervals,

$$\begin{aligned}
(-\Theta, \Theta) &: \left|\frac{b}{c}\right| > |K(\theta)| \\
(\Theta, -\Theta) &: \left|\frac{b}{c}\right| < |K(\theta)|
\end{aligned} \tag{34}$$

Now we can simplify the $W$ integral into the form of Eq. (9) in [15], for $c \geq b \geq a$.

$$\begin{aligned}
W &= \ln c + \oiint \frac{d\theta d\phi}{4\pi^2}\ln\left(1 - \frac{a}{c}e^{-i\theta} - \frac{b}{c}e^{i\phi}\right) \\
&= \ln c + \frac{1}{2\pi}\left(\int_{-\Theta}^{\Theta}\ln\left(\frac{b}{c}\right)d\theta + \int_{\Theta}^{-\Theta}\ln\left(1 - \frac{a}{c}e^{-i\theta}\right)d\theta\right) \\
&= \ln c + \frac{\Theta}{\pi}\ln\left(\frac{b}{c}\right) + \frac{1}{2\pi}\int_{\Theta}^{-\Theta}\ln\left(1 - \frac{a}{c}e^{-i\theta}\right)d\theta
\end{aligned} \tag{35}$$

Now using the substitution $u = \frac{a}{c}e^{-i\theta}$, one obtains the final form:

$$\begin{aligned} W &= \ln c + \frac{\Theta}{\pi}\ln\left(\frac{b}{c}\right) - \frac{1}{2\pi i}\int_{\frac{a}{c}e^{-i\Theta}}^{\frac{a}{c}e^{i\Theta}} \frac{\ln(1-u)}{u}du \\ &= \ln c + \frac{\Theta}{\pi}\ln\left(\frac{b}{c}\right) + \frac{1}{2\pi i}\left(-\int_0^{\frac{a}{c}e^{i\Theta}} \frac{\ln(1-u)}{u}du + \int_0^{\frac{a}{c}e^{-i\Theta}} \frac{\ln(1-u)}{u}du\right) \\ &= \ln c + \frac{\Theta}{\pi}\ln\left(\frac{b}{c}\right) + \frac{1}{2\pi i}\left(li_2\left(\frac{a}{c}e^{i\Theta}\right) - li_2\left(\frac{a}{c}e^{-i\Theta}\right)\right) \end{aligned} \tag{36}$$

This quantity is can be used to compute important thermodynamic properties of the system, such as the Helmholtz free energy per dimer $\mathcal{F} = -\frac{1}{\beta}W$, the internal energy per dimer $U = -\frac{\partial W}{\partial \beta}$ and the specific heat capacity $C = \beta^2\frac{\partial^2 W}{\partial \beta^2}$. A special case for $W$ is where one of these weights $a, b$ or $c$ is larger than the sum of the other two. In this case, the value of $W$ will simply be the natural logarithm of that weight, that is, $W = \ln(\max(a, b, c))$. This can be seen by applying the identity in Eq. (32) to the two separate integrals. These regions, namely $W = \ln a$, $W = \ln b$, and $W = \ln c$ are called frozen regions, and in these regions the lattice is totally ordered and consists purely of dimers across the bonds with the largest weight. Hence, at the point where one weight is equal to the sum of the other two, there is a phase transition. It has been shown to be a one-sided second-order (or one-sided continuous) phase transition, and is often referred to as a $\frac{3}{2}$-order transition. All of this behaviour has been discussed in [15] and related works such as [17] and [18]. We can see this by plotting thermodynamic quantities for $c = 1$ and $a = b = e^{-\beta}$.

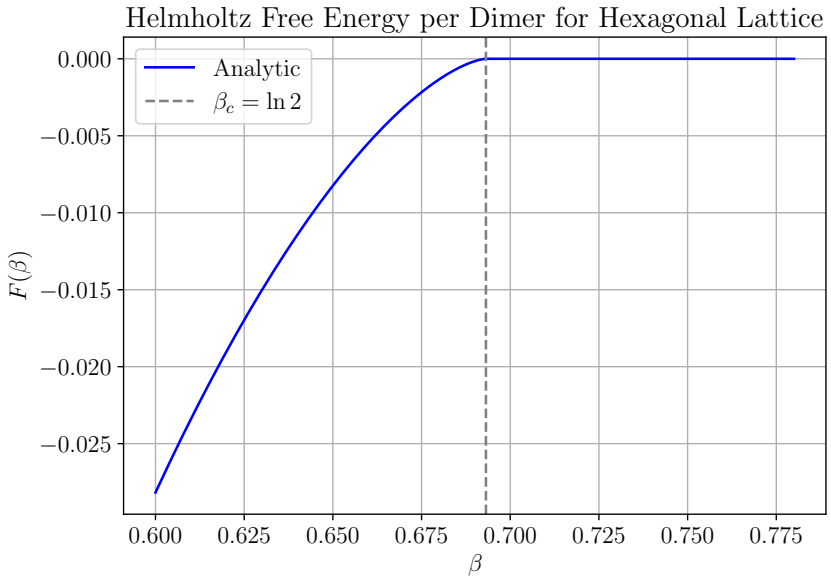



Figure 9: *Plot of the Helmholtz Free Energy per Dimer for the bipartite hexagonal lattice, with bond activities* $c = 1$, $a = b = e^{-\beta}$.

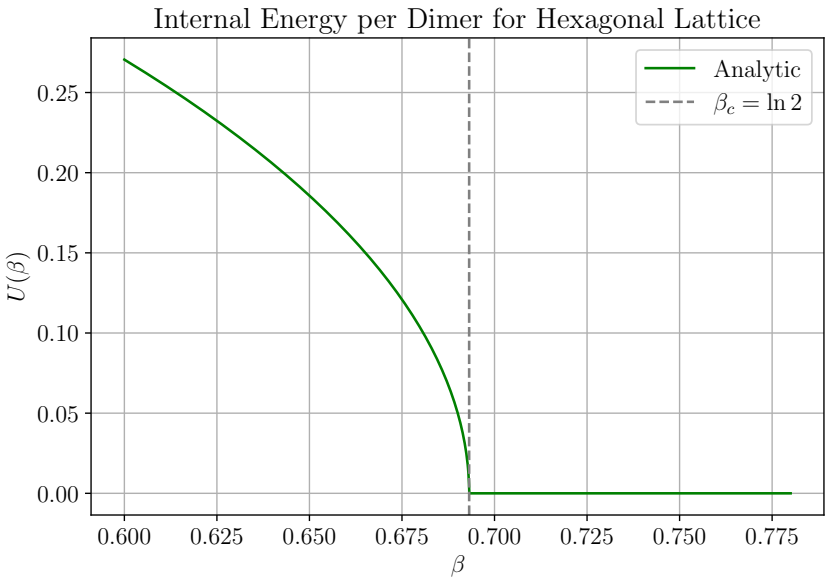



Figure 10: *Plot of the Internal Energy per Dimer for the bipartite hexagonal lattice, with bond activities* $c = 1$, $a = b = e^{-\beta}$.

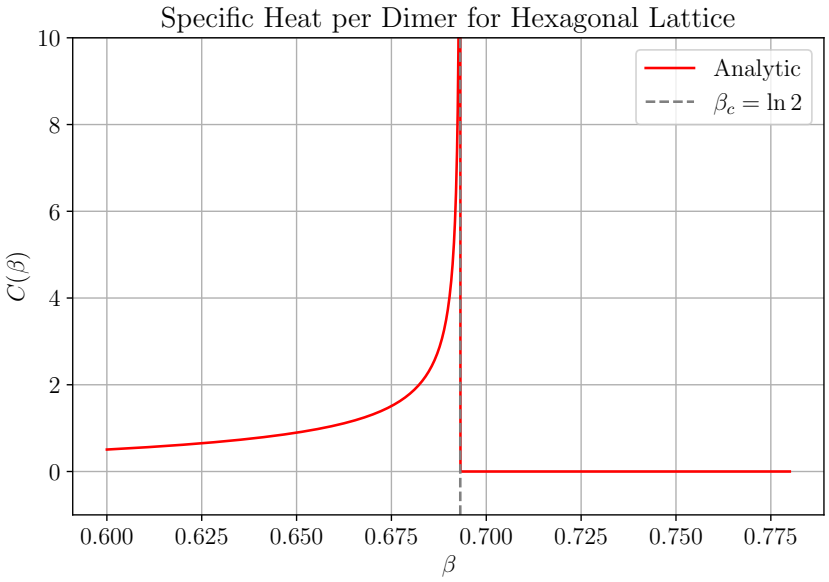



Figure 11: *Plot of the Specific Heat Capacity for the bipartite hexagonal lattice, with bond activities* $c = 1$, $a = b = e^{-\beta}$.

# 4 The Square-Triangle Lattice

Having looked at a bipartite hexagonal lattice, we wish to consider the effect of making this non-bipartite, by adding in "$d$" bonds between horizontally adjacent black vertices and "$e$" bonds between horizontally adjacent white vertices. We will call this the square-triangle lattice from now on. We need to also ensure that we still have a valid Kasteleyn orientation on the lattice, which is done by assigning the bonds the directions shown in Fig. 12. This will, of course, give a different Kasteleyn matrix from the one in the bipartite case. While the partition function on a genus-$g$ surface is still given by Eq. (6), the special block off-diagonal form of $K$ in the bipartite case is absent here. In the bipartite setting, this structure seen in

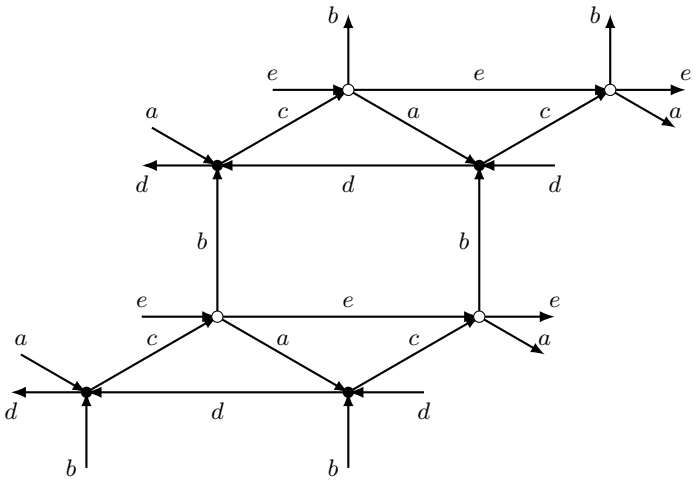



Figure 12: *Small example of our square-triangle lattice, showing activities of the different bonds and our choice of Kasteleyn orientation.*

Eq. (4) arises from a chirality property:

$$\Gamma K + K\Gamma = 0, \quad \Gamma = \begin{pmatrix} \mathbb{1} & 0 \\ 0 & -\mathbb{1} \end{pmatrix}, \tag{37}$$

where $\mathbb{1}$ is the identity matrix of dimension equal to that of $A$. This property implies $\mathrm{Pf}(K) = \det(A)$, leading to a simplification of the partition function in the bipartite case. In the non-bipartite setting, this chirality is lost, and such a determinant reduction is no longer possible. We still wish to get an expression similar to that in Eq. (28) by Fourier transforming the matrix. This reduces the determinant of the Kasteleyn matrix to the following:

$$\begin{aligned} \det(K) &= \prod_{n,m=1}^{N,M} \det \begin{pmatrix} -d\left(e^{2\pi i n/N} - e^{-2\pi i n/N}\right) & c - ae^{-2\pi i n/N} - be^{2\pi i m/M} \\ -\left(c - ae^{2\pi i n/N} - be^{-2\pi i m/M}\right) & \mathbf{e}\left(e^{2\pi i n/N} - e^{-2\pi i n/N}\right) \end{pmatrix} \\ &= \prod_{n,m=1}^{N,M} \left( 4\mathbf{e}d \sin^2\left(\frac{2\pi n}{N}\right) + \left| p^{\mathrm{Hex}}\left(e^{2\pi i n/N}, e^{2\pi i m/M}\right) \right|^2 \right) \end{aligned} \tag{38}$$

Here $\mathbf{e}$ is the activity of the bond and has been made bold to distinguish it from Euler's number. Also $p^{\mathrm{Hex}}$ is the spectral polynomial given in Eq. (26). We now want to find the zeros of this new equation, which looks like the following in terms of $\theta_n$ and $\phi_m$:

$$p^{\mathrm{ST}}(\theta_n, \phi_m) = 4ed \sin^2\theta_n + \left| p^{\mathrm{Hex}}\left(e^{i\theta_n}, e^{i\phi_m}\right) \right|^2 \tag{39}$$

[3] Since both terms of this equation are positive definite, there will be no ambiguity when we wish to take the square root later on, and we know they must both go to zero separately. Just looking at the first term, the zero angle $\Theta$ must be either 0 or $\pi$. Now we can use the previous result for the zeros of $p^{\mathrm{Hex}}(e^{i\theta}, e^{i\phi})$, namely we recall that

$$\sin\Theta = \frac{b}{2r} = \frac{\sqrt{(a+b+c)(-a+b+c)(a-b+c)(a+b-c)}}{2ac} \tag{40}$$

Since the first term gave us the fact that $\sin\Theta = 0$, we need a further restriction on the values of $a$, $b$ and $c$ to ensure this. There are three cases:

$$\begin{aligned} &\textbf{Case 1}\text{: } c = a + b \implies \Theta = \Phi = 0 \\ &\textbf{Case 2}\text{: } a = b + c \implies \Theta = 0,\ \Phi = \pi \\ &\textbf{Case 3}\text{: } b = a + c \implies \Theta = \pi,\ \Phi = 0 \end{aligned} \tag{41}$$

[3] Again, for the rest of this section these angles will simply be denoted by $\theta$ and $\phi$ as we take the continuum limit.

Notice that in this non-bipartite case, there is only one zero in each of these cases due to the fact that $(\Theta, \Phi) = (-\Theta, -\Phi)$, compared to previously in the bipartite case where there was two zeros. Now we wish to once again compute the free energy per dimer for one of these cases. The full integral in the continuum limit looks like the following:

$$\begin{aligned} W &= \frac{1}{2} \iint_{\mathbb{D}} \frac{d\theta d\phi}{4\pi^2} \ln\left(p^{\mathrm{ST}}(\theta, \phi)\right) \\ &= \frac{1}{2} \iint_{\mathbb{D}} \frac{d\theta d\phi}{4\pi^2} \ln\left(4ed\sin^2\theta + c^2 + a^2 + b^2 - 2c(a\cos\theta + b\cos\phi) + 2ab\cos(\theta - \phi)\right) \end{aligned} \tag{42}$$

Note that the extra factor of $\frac{1}{2}$ was needed here since we are using the Pfaffian of $K$, which is the square root of the determinant. Using $\cos\phi = \frac{1}{2}(w + w^{-1})$ and $\cos(\theta - \phi) = \frac{1}{2}(z/w + w/z)$, one finds $p^{\mathrm{ST}}(\theta, \phi)$ is linear in $w$ and $w^{-1}$. Collecting powers of $w$ one finds

$$p^{\mathrm{ST}}(\theta, \phi) = \alpha(z) + \beta(z)\, w + \gamma(z)\, w^{-1}, \tag{43}$$

with the $\theta$-dependent coefficients

$$\begin{aligned} \beta(z) &= \frac{ab}{z} - bc, \\ \gamma(z) &= ab\, z - bc, \\ \alpha(z) &= a^2 - ac\big(z + z^{-1}\big) + b^2 + c^2 + 2de - de\big(z^2 + z^{-2}\big), \end{aligned} \tag{44}$$

which follow directly from expanding $p^{\mathrm{ST}}$ after substituting $z, w$. Multiplying by $w$ yields the quadratic polynomial

$$w\, p^{\mathrm{ST}}(\theta, \phi) = \beta(z)\, w^2 + \alpha(z)\, w + \gamma(z)) \tag{45}$$

Denote the two roots by $r_{1,2}(z)$, so that

$$\beta(z)\, w^2 + \alpha(z)\, w + \gamma(z) = \beta(z)\big(w - r_1(z)\big)\big(w - r_2(z)\big). \tag{46}$$

The two roots are given explicitly by the quadratic formula

$$r_{1,2}(z) = \frac{-\alpha(z) \pm \sqrt{\alpha(z)^2 - 4\beta(z)\gamma(z)}}{2\beta(z)}. \tag{47}$$

Therefore

$$\ln p^{\mathrm{ST}}(\theta, \phi) = \ln\beta(z) + \ln\left(w - r_1(z)\right) + \ln\left(w - r_2(z)\right) - \ln w. \tag{48}$$

Since $\ln\left(p^{\mathrm{ST}}(\theta, \phi)\right) = \ln\left|p^{\mathrm{ST}}(\theta, \phi)\right|$ for real and positive weights and using the identity in Eq. (32), we obtain the $\phi$-averaged integrand

$$I(\theta) \equiv \frac{1}{2\pi} \int_0^{2\pi} \ln\left(p^{\mathrm{ST}}(\theta, \phi)\right)\, d\phi = \ln\left|\beta(z)\right| + \ln\max\{1, |r_1(z)|\} + \ln\max\{1, |r_2(z)|\}. \tag{49}$$

Finally, we can write $W$ as a single integral:

$$W \;=\; \frac{1}{2} \int_0^{2\pi} \frac{d\theta}{2\pi}\, I(\theta) \;=\; \frac{1}{2} \int_0^{2\pi} \frac{d\theta}{2\pi} \left[ \ln\left|\beta(z)\right| + \sum_{j=1}^{2} \ln\max\{1, |r_j(z)|\} \right] \tag{50}$$

Here $z = e^{i\theta}$, $\beta(z) = \dfrac{ab}{z} - bc$, and $r_{1,2}(z)$ are the roots of $\beta(z)w^2 + \alpha(z)w + \gamma(z) = 0$ with $\alpha, \gamma$ as above. In practice one evaluates the integrand at each $\theta$ by forming $\beta, \alpha, \gamma$, solving the quadratic, taking the moduli of the roots, and then integrating numerically in $\theta$. What we expect to see is some form of phase transition at the point where one of $a$, $b$ or $c$ is the sum of the other two, similar to the bipartite case. Taking **Case 1** in Eq. (41), we parametrise the weights in the following way:

$$\begin{aligned} c = e = d &= 1 \\ a = b &= e^{-\beta} \end{aligned} \tag{51}$$

Since the critical point is when $c = a + b$, then we expect $\beta_c = \ln 2$. The numerical plots of some thermodynamic properties of the system are shown in the figures below. It should be noted that for all plots in this report, $\Delta = \beta - \beta_c$.

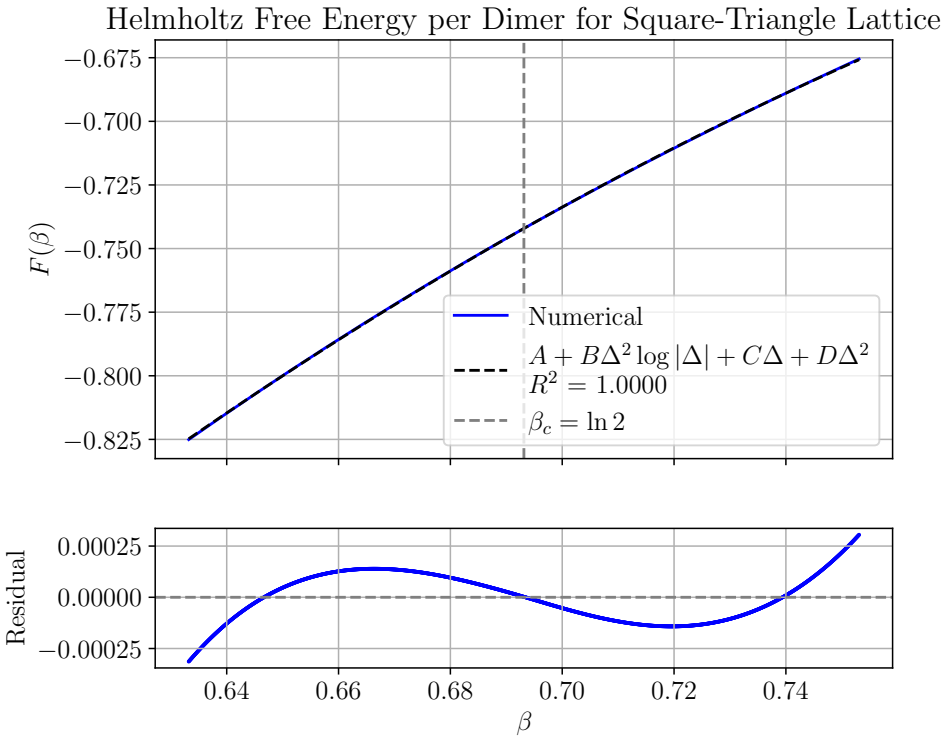



Figure 13: *Plot of the Helmholtz Free Energy per Dimer for the square-triangle lattice, with bond activities* $c = d = e = 1$, $a = b = e^{-\beta}$ *and* $\Delta = \beta - \beta_c$.

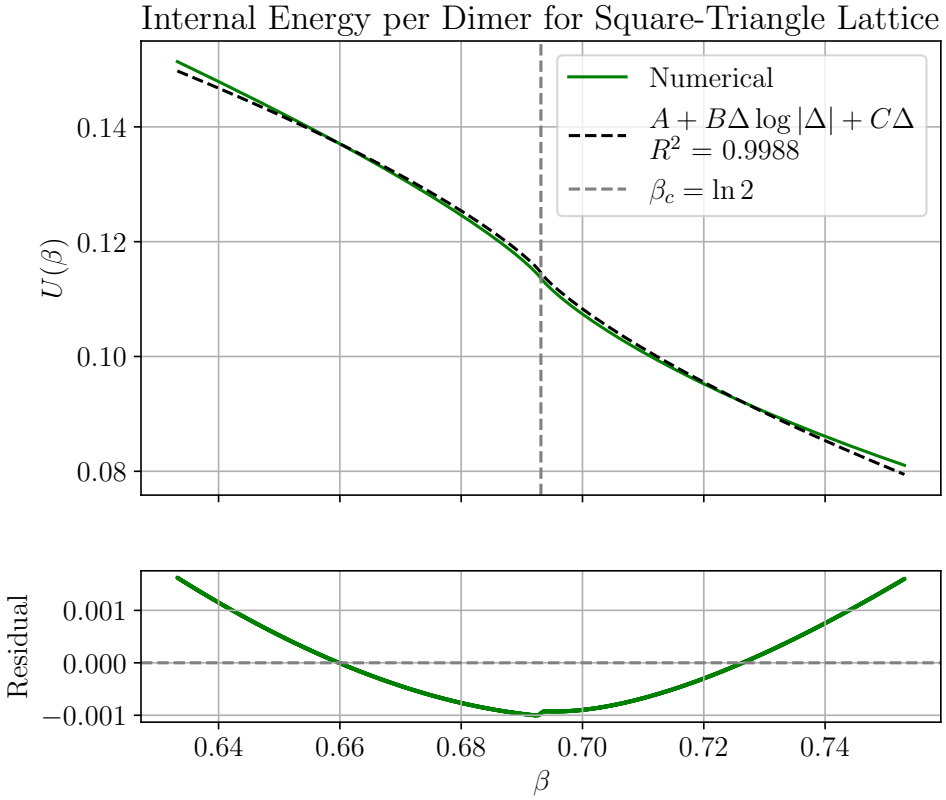



Figure 14: *Plot of the Internal Energy per Dimer for the square-triangle lattice, with bond activities* $c = d = e = 1$, $a = b = e^{-\beta}$ *and* $\Delta = \beta - \beta_c$.

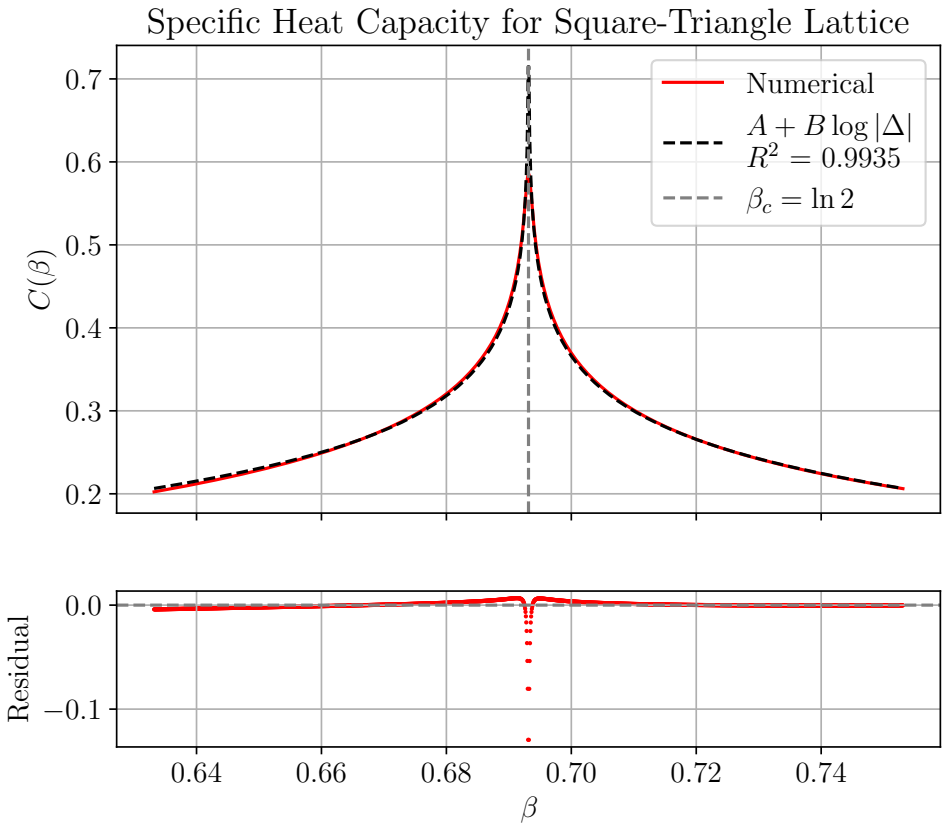



Figure 15: *Plot of the Specific Heat Capacity for the square-triangle lattice, with bond activities* $c = d = e = 1$, $a = b = e^{-\beta}$ *and* $\Delta = \beta - \beta_c$. *It should be noted that* $A$ *and* $B$ *which are fit here can be obtained analytically with effort, but time did not permit it for this current write-up.*

As can be seen by the plots in Figures 13, 14 and 15, there is a continuous or second order phase transition at the critical point $\beta_c = \ln 2$ as predicted. It can also be seen that the divergence of the specific heat capacity is logarithmic in nature and symmetric about the critical point, implying that this square-triangle lattice is in the same universality class as the Ising model. We can check the symmetric nature of this divergence, which is shown in Table 2. Here $\Delta\beta$ is the offset from $\beta_c$. $\Delta C$ denotes the absolute difference $\Delta C = |C(\beta_c + \Delta\beta) - C(\beta_c - \Delta\beta)|$, and $\delta C_{\text{rel}}$ is the relative difference

$$\delta C_{\text{rel}} = \frac{\Delta C}{\max\left(|C(\beta_c + \Delta\beta)|,\ |C(\beta_c - \Delta\beta)|\right)}. \tag{52}$$

As can be seen in the table, the divergence of the specific heat capacity is symmetric about the critical point up to numerical error. We can also compute the modular parameter for the case $c = a + b$ we have considered. This is done by expanding $p^{\text{ST}}$ around the critical angles $\Theta = \Phi = 0$.

$$\begin{aligned} p^{\text{ST}}(\theta,\phi) &= 4de\sin^2\theta + \left|p^{\text{Hex}}(e^{i\theta}, e^{i\phi})\right|^2 \\ &\approxeq 4de\theta^2 + \left|c - a(1 - i\theta) - b(1 + i\phi)\right|^2 \\ &= 4de\theta^2 + \left|i(a\theta - b\phi)\right|^2 \\ &= (4de + a^2)\theta^2 - 2ab\theta\phi + b^2\phi^2 \end{aligned} \tag{53}$$

Now we can use the original full definitions of $\theta = \frac{2\pi(n+u)}{N}$ and $\phi = \frac{2\pi(m+v)}{M}$,

$$\begin{aligned} p^{\text{ST}}(\theta,\phi) \approxeq \left(\frac{2\pi}{N}\right)^2 (a^2 + 4de)\Bigg[(n+u)^2 - \frac{2abN}{(a^2+4de)M}(n+u)(m+v) + \\ + \frac{1}{a^2+4de}\left(\frac{bN}{M}\right)^2 (m+v)^2\Bigg] \end{aligned} \tag{54}$$

| $\Delta\beta$ | $C(\beta_c - \Delta\beta)$ | $C(\beta_c + \Delta\beta)$ | $\Delta C$ | $\delta C_{\text{rel}}$ |
|---|---|---|---|---|
| 0.0010 | 0.512750 | 0.512549 | $2.013 \times 10^{-4}$ | $3.926 \times 10^{-4}$ |
| 0.0038 | 0.415391 | 0.414924 | $4.676 \times 10^{-4}$ | $1.126 \times 10^{-3}$ |
| 0.0066 | 0.373401 | 0.372822 | $5.795 \times 10^{-4}$ | $1.552 \times 10^{-3}$ |
| 0.0094 | 0.346415 | 0.345812 | $6.025 \times 10^{-4}$ | $1.739 \times 10^{-3}$ |
| 0.0121 | 0.326482 | 0.325918 | $5.637 \times 10^{-4}$ | $1.727 \times 10^{-3}$ |
| 0.0149 | 0.310656 | 0.310178 | $4.779 \times 10^{-4}$ | $1.538 \times 10^{-3}$ |
| 0.0177 | 0.297522 | 0.297168 | $3.542 \times 10^{-4}$ | $1.191 \times 10^{-3}$ |
| 0.0205 | 0.286286 | 0.286087 | $1.992 \times 10^{-4}$ | $6.957 \times 10^{-4}$ |
| 0.0233 | 0.276463 | 0.276446 | $1.723 \times 10^{-5}$ | $6.232 \times 10^{-5}$ |
| 0.0261 | 0.267730 | 0.267918 | $1.880 \times 10^{-4}$ | $7.017 \times 10^{-4}$ |
| 0.0289 | 0.259865 | 0.260279 | $4.138 \times 10^{-4}$ | $1.590 \times 10^{-3}$ |
| 0.0316 | 0.252707 | 0.253365 | $6.577 \times 10^{-4}$ | $2.596 \times 10^{-3}$ |
| 0.0344 | 0.246136 | 0.247054 | $9.181 \times 10^{-4}$ | $3.716 \times 10^{-3}$ |
| 0.0372 | 0.240059 | 0.241252 | $1.193 \times 10^{-3}$ | $4.946 \times 10^{-3}$ |
| 0.0400 | 0.234405 | 0.235887 | $1.482 \times 10^{-3}$ | $6.282 \times 10^{-3}$ |

Table 2: *Symmetry check for $C(\beta)$ for the square-triangle lattice around $\beta_c = \ln 2$.*

We can now compare this with the following to find the modular parameter $\tau$:

$$\begin{aligned} p(n,m) &\sim [(n+u)+\tau(m+v)]\,[(n+u)+\bar{\tau}(m+v)] \\ &= (n+u)^2 + (\tau+\bar{\tau})(m+v)(n+u) + \tau\bar{\tau}(m+v)^2 \end{aligned} \tag{55}$$

Taking $\tau = \tau_0 + i\tau_1$ gives two equations:

$$\begin{aligned} \tau + \bar{\tau} = 2\tau_0 \implies \tau_0 &= \frac{abN}{(a^2+4de)M} \\ \tau\bar{\tau} = \tau_0^2 + \tau_1^2 \implies \tau_1 &= \frac{2bN\sqrt{de}}{(a^2+4de)M} \end{aligned} \tag{56}$$

Combining these gives the result that

$$\tau = \frac{bN}{M(a^2+4de)}\left(a + 2i\sqrt{de}\right) \tag{57}$$

Eq. (57) constitutes a new result of this work. It can be directly compared to equation (20) of Ref. [15], "Topological phase transitions and holonomies in the dimer model", for the bipartite hexagonal lattice with positive weights $a$, $b$ and $c$. This is shown below:

$$\lim_{N,M\to\infty} \frac{\mathcal{Z}(N,M)}{e^{NMW(a,b,c)}} = \mathcal{Z}_{Dirac}(\theta,\phi,\tau) = \frac{1}{2}\sum_{u,v=0}^{1/2} \left| \frac{\theta[{}^{\theta+u}_{\phi+v}](0|\tau)}{\eta(\tau)} \right| \tag{58}$$

Upon specialising to the case $\theta = 0,\ \phi = 0$ for this new case, the result is:

$$\lim_{N,M\to\infty} \frac{\mathcal{Z}(N,M)}{e^{NMW(a,b,c,d,e)}} = \frac{1}{2}\sum_{u,v=0}^{1/2} \left| \frac{\theta[{}^{u}_{v}](0|\tau)}{\eta(\tau)} \right|^{\frac{1}{2}} \tag{59}$$

where the power of $1/2$ of the theta function arises from taking the square root of the determinant of the Kateleyn matrix. The parameter $\tau$ in Eq. (57) is the modular parameter in the toroidal geometry of the dimer model. Notably:

- In the limit $d \to 0$ or $e \to 0$, we have $\mathrm{Im}(\tau) \to 0$, and the torus degenerates into a collapsed geometry.
- For any finite, non-zero $d$ and $e$, $\mathrm{Im}(\tau) > 0$, corresponding to a non-degenerate torus geometry with well-defined modular properties.

This correspondence highlights that Eq. (57) extends the modular-geometric interpretation of the bipartite dimer model to the present non-bipartite setting with additional $d$ and $e$ bonds. The appearance of the sum over theta functions with the square root in Eq. (59) is precisely the structure of the conformal character decomposition in the Ising conformal field theory. The factor of $1/2$ in the exponent modifies the standard Dirac fermion partition function to that of a single free Majorana fermion, corresponding to the Ising model CFT with central charge $c = \frac{1}{2}$. This not only provides a concrete and essentially rigorous identification of the present non-bipartite dimer model with additional $d$ and $e$ bonds as belonging to the universality class of the two-dimensional Ising model, but also offers a direct connection to Majorana fermions. From this perspective, the bipartite case can be viewed as describing two Majorana fermions of opposite chirality, which together form a Dirac fermion. In the bipartite Kasteleyn matrix, this chiral decomposition is captured by the anticommutation relation shown in Eq. (37). The projectors $(1 + \Gamma)/2$ and $(1 - \Gamma)/2$ isolate the distinct chiral components. In the non-bipartite setting considered here, this chirality structure is lost, leaving only a single Majorana sector in the continuum limit. The concept that this non-bipartite dimer model is in the same universality class as the two-dimensional Ising model implies that the large-scale, long-distance behaviour of the system — including its critical exponents, scaling functions, and operator content [19] — is identical to that of the two-dimensional Ising model, independent of microscopic details such as the precise values of $d$ and $e$, provided they are non-zero.

# 5 The Triangular Lattice

Having verified Ising-like behaviour for the square-triangle lattice, we want to see if this behaviour is also seen in other non-bipartite lattices. Namely we wish to study the behaviour of a triangular lattice near a critical point. The easiest way to do this is adding in another bond, which we will denote by activity $f$, to our square-triangle lattice. This is shown in Fig. 16. It should be noted that the inclusion of

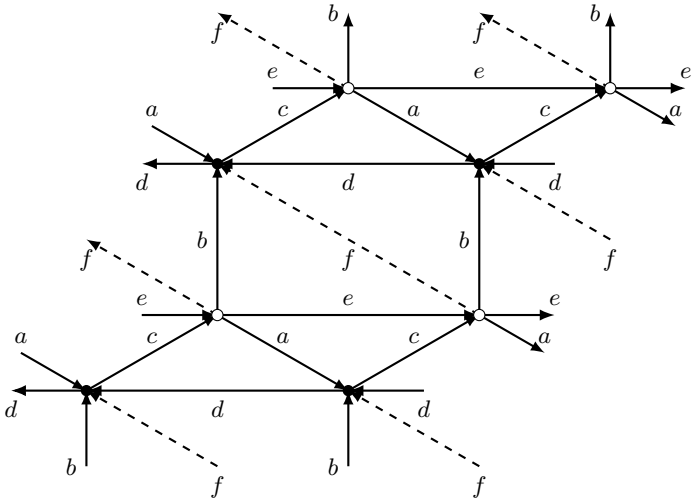



Figure 16: *Small example of our triangular lattice, showing activities of the different bonds and our choice of Kasteleyn orientation. The dashed arrows indicate the $f$ bonds, i.e. the bonds that were added in to the square-triangle lattice in Fig. 12.*

the additional $f$ bond does not break the bipartite nature of the lattice. Moreover, by setting $d = 0$ and $e = 0$ the resulting tiling corresponds to a "square" lattice (up to a visual straightening of the bonds), thus incorporating the square-lattice dimer model as a special case within our framework. This will once again give a different Katelyn matrix, but it is similar to that of the square-triangle lattice. The determinant is given by the following, where again $\theta_n = \frac{2\pi n}{N}$ and $\phi_m = \frac{2\pi m}{M}$.

$$\begin{aligned}\det(K) &= \prod_{n,m=1}^{N,M} \det \begin{pmatrix} -d\left(e^{i\theta_n} - e^{-i\theta_n}\right) & p^{\text{Hex}}\left(e^{i\theta_n}, e^{i\phi_m}\right) - fe^{i(\theta_n+\phi_m)} \\ -\left(p^{\text{Hex}}\left(e^{-i\theta_n}, e^{-\phi_m}\right) - fe^{-i(\theta_n+\phi_m)}\right) & \mathbf{e}\left(e^{i\theta_n} - e^{-i\theta_n}\right) \end{pmatrix} \\ &= \prod_{n,m=1}^{N,M} \left(4\mathbf{e}d\sin^2\left(\frac{2\pi n}{N}\right) + \left|p^{\text{Hex}}\left(e^{2\pi i n/N}, e^{2\pi i m/M}\right) - fe^{2\pi i(n/N+m/M)}\right|^2\right)\end{aligned} \tag{60}$$

This gives us yet another equation to find the zeros of, which is given in Eq. (61).

$$p^{\text{Tri}}(\theta_n, \phi_m) = 4ed\sin^2\theta_n + \left|p^{\text{Hex}}\left(e^{i\theta_n}, e^{i\phi_m}\right) - fe^{i(\theta_n+\phi_m)}\right|^2 \tag{61}$$

[4] Like before, since both of these terms are positive definite, they most be zero separately, meaning we have either $\Theta = 0$ or $\Theta = \pi$. Take the first case $\Theta = 0$, now we the following for the second term:

$$p^{\text{Hex}}(1, e^{i\phi}) - fe^{i\phi} = c - a - (b+f)e^{i\phi} \tag{62}$$

Since this must be zero we have two sub cases, which gives us our first two possible restrictions for there to be a zero of this equation:

$$\begin{aligned} &\textbf{Case 1: } \Theta = \Phi = 0 \implies c = a + b + f \\ &\textbf{Case 2: } \Theta = 0,\ \Phi = \pi \implies a = c + b + f \end{aligned} \tag{63}$$

Employing a similar strategy for $\Theta = \pi$ gives two more cases for the existence of a zero, namely:

$$\begin{aligned} &\textbf{Case 3: } \Theta = \pi,\ \Phi = 0 \implies b = c + a + f \\ &\textbf{Case 4: } \Theta = \Phi = \pi \implies f = c + a + b \end{aligned} \tag{64}$$

Again, there is only one zero for these cases, similar to square-triangle lattice. We again wish to compute the free energy per dimer which is given by the following:

$$\begin{aligned} W &= \frac{1}{2}\iint \frac{d\theta d\phi}{4\pi^2} \ln\left(p^{\text{Tri}}(\theta,\phi)\right) \\ &= \frac{1}{2}\iint \frac{d\theta d\phi}{4\pi^2} \ln\big(4ed\sin^2\theta + c^2 + a^2 + b^2 + f^2 - 2c(a\cos\theta + b\cos\phi + f\cos(\theta+\phi)) + \\ &+ 2ab\cos(\theta-\phi) + 2f(a\cos(2\theta+\phi) + b\cos\theta\big) \end{aligned} \tag{65}$$

In an attempt to reduce this double integral to a single integral, we define

$$\alpha(\theta) := c - ae^{-i\theta}, \tag{66}$$

$$\beta(\theta) := -b - fe^{i\theta}. \tag{67}$$

Then, as a function of $w = e^{i\phi}$,

$$K(\theta, w) \ := \ p^{\text{Hex}}(e^{i\theta}, w) - fe^{i\theta}w = \alpha(\theta) + \beta(\theta)\, w.$$

Hence

$$\left|K(\theta,w)\right|^2 \ = \ |\alpha|^2 + |\beta|^2 + \overline{\alpha}\beta\, w + \alpha\overline{\beta}\, w^{-1}.$$

Define the functions

$$A(\theta) := 4de\sin^2\theta + |\alpha(\theta)|^2 + |\beta(\theta)|^2, \tag{68}$$

$$B(\theta) := \overline{\alpha(\theta)}\,\beta(\theta). \tag{69}$$

Then

$$p^{\text{Tri}}(\theta,\phi) = A(\theta) + B(\theta)e^{i\phi} + \overline{B(\theta)}e^{-i\phi} = A(\theta) + 2|B(\theta)|\cos\left(\phi + \arg B(\theta)\right). \tag{70}$$

We now use the standard identity (valid for real $A \geq 2|B|$)

$$\int_0^{2\pi} \ln\big(A + 2|B|\cos\phi\big)\, d\phi = 2\pi \ln\Big(\frac{A + \sqrt{A^2 - 4|B|^2}}{2}\Big). \tag{71}$$

Applying this to the $\phi$ integral gives a dramatic simplification: the double integral for the free-energy density becomes a single $\theta$–integral,

$$W \ = \ \frac{1}{2}\frac{1}{(2\pi)^2}\int_0^{2\pi} d\theta \int_0^{2\pi} \ln\left(p^{\text{Tri}}(\theta,\phi)\right)\, d\phi \ = \ \frac{1}{4\pi}\int_0^{2\pi} \ln\left[\frac{A(\theta) + \sqrt{A(\theta)^2 - 4|B(\theta)|^2}}{2}\right] d\theta. \tag{72}$$

A couple of remarks:

[4] Again, for the rest of this section these angles will simply be denoted by $\theta$ and $\phi$ as we take the continuum limit.

- $A(\theta) \geq 2|B(\theta)|$ for all $\theta$, hence the square root is manifestly real and positive and the integrand is the real logarithm shown above. A short derivation of this is given here:

$$\begin{aligned} A \geq 2|B| &\iff A^2 - 4|B|^2 \geq 0 \\ &\iff (A + 2|B|)(A - 2|B|) \geq 0 \\ &\iff A - 2|B| \geq 0 \\ &\iff 4ed\sin^2\theta + (|\alpha| - |\beta|)^2 \geq 0 \end{aligned} \tag{73}$$

- The only problem area here is for $A(\theta) = |B(\theta)| = 0$, which correspond to the special cases in Eq. (63) and (64). These special cases manifest themselves in the phase transitions seen in the plots below. At this point one hits the branch cut in the integrand over $\theta$, and it is this that gives the singularity of the specific heat. At this point, the discriminant

$$Q(\theta) := A(\theta)^2 - 4|B(\theta)|^2 \tag{74}$$

  is also zero. At $\theta = 0$ one finds

$$Q(0) = (-a + b + c + f)^2(a + b + f - c)^2, \tag{75}$$

  while at $\theta = \pi$,

$$Q(\pi) = (a - b + c + f)^2(a + b + c - f)^2. \tag{76}$$

  At criticality one of these factors vanishes, so $Q(\theta)$ has no constant term. A small–$\theta$ expansion then gives

$$Q(\theta) = 16(a - c)^2 de\,\theta^2 + O(\theta^3) \qquad (\theta \to 0), \tag{77}$$

  and

$$Q(\theta) = 16(a + c)^2 de\,(\pi - \theta)^2 + O((\pi - \theta)^3) \qquad (\theta \to \pi). \tag{78}$$

  These vanishing quadratics are what produce the logarithmic singularity in the free energy and the corresponding divergence in the specific heat.

- Eq. (72) reduces the original double integral to a single well-conditioned one-dimensional integral and is the exact triangular-lattice analogue of the reduction used for the square-triangle (hexagonal-based) case.

We now wish to compute this numerically for a given choice of bond activities. In an attempt to study **Case 1** in Eq. (63). We parametrise the weights by the following:

$$\begin{aligned} c = e = d = 1 \\ a = b = f = e^{-\beta} \end{aligned} \tag{79}$$

Since the critical point for this case is when $c = a + b + f$, we expect that $\beta_c = \ln 3$ will be the critical point for this phase transition. The relevant thermodynamic properties for the triangular lattice were again plotted and are shown below.

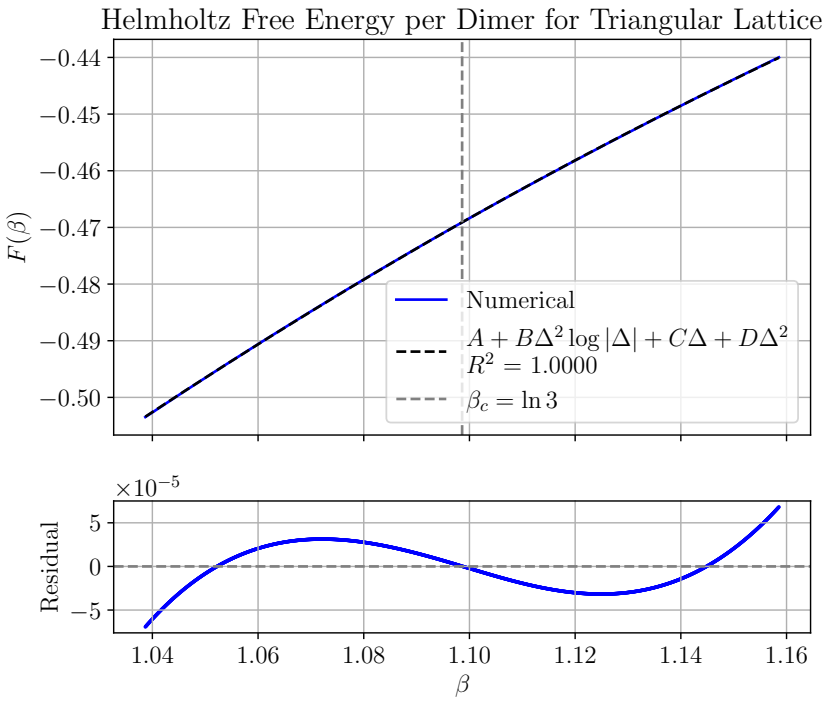



Figure 17: *Plot of the Helmholtz Free Energy per Dimer for the triangular lattice, with bond activities* $c = d = e = 1$, $a = b = f = e^{-\beta}$ *and* $\Delta = \beta - \beta_c$.

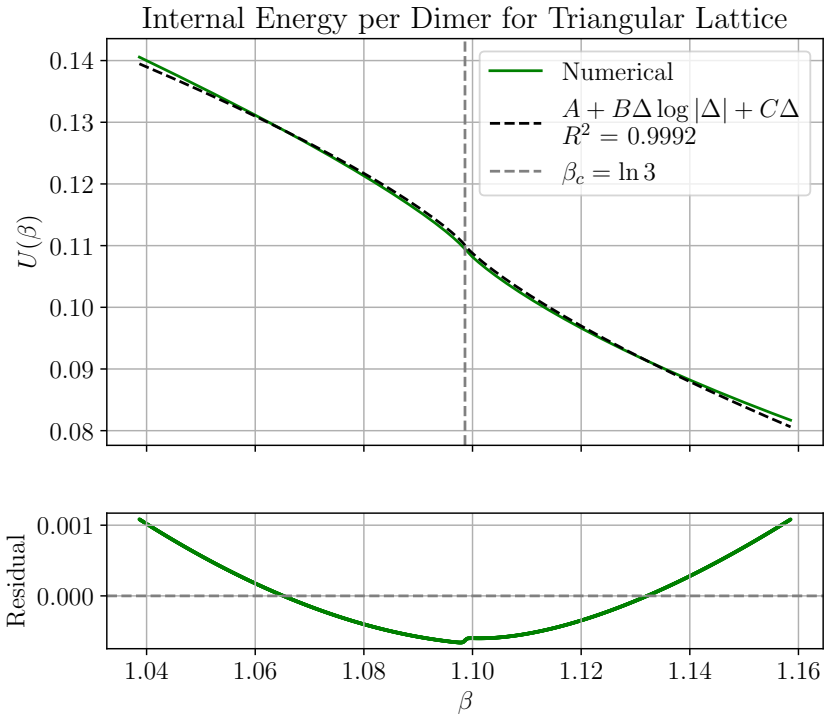



Figure 18: *Plot of the Internal Energy per Dimer for the triangular lattice, with bond activities* $c = d = e = 1$, $a = b = f = e^{-\beta}$ *and* $\Delta = \beta - \beta_c$.

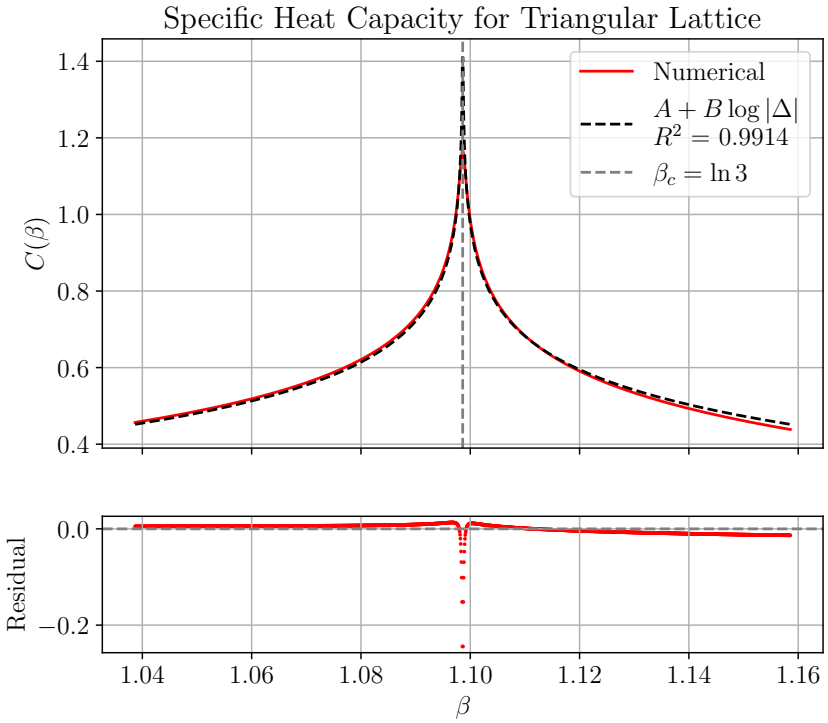



Figure 19: *Plot of the Specific Heat Capacity for the triangular lattice, with bond activities* $c = d = e = 1$, $a = b = f = e^{-\beta}$ *and* $\Delta = \beta - \beta_c$. *It should again be noted that* $A$ *and* $B$ *which are fit here can be obtained analytically with effort, but time did not permit it for this current write-up.*

These plots are similar to those of the other non-bipartite lattice. It can once again be seen that there is a second-order or continuous phase transition at the critical point $\beta_c = \ln 3$. The divergence at this point is also logarithmic in nature, indicating that this dimer model is also in the same universality class as the Ising model. As can be seen in Table 3, the divergence of the specific heat capacity is again symmetric about the critical point up to numerical error.

| $\Delta\beta$ | $C(\beta_c - \Delta\beta)$ | $C(\beta_c + \Delta\beta)$ | $\Delta C$ | $\delta C_{\text{rel}}$ |
|---|---|---|---|---|
| 0.0010 | 1.029404 | 1.028329 | $1.075 \times 10^{-3}$ | $1.044 \times 10^{-3}$ |
| 0.0038 | 0.846757 | 0.843604 | $3.153 \times 10^{-3}$ | $3.724 \times 10^{-3}$ |
| 0.0066 | 0.768357 | 0.763557 | $4.800 \times 10^{-3}$ | $6.247 \times 10^{-3}$ |
| 0.0094 | 0.718188 | 0.711978 | $6.210 \times 10^{-3}$ | $8.646 \times 10^{-3}$ |
| 0.0121 | 0.681283 | 0.673827 | $7.456 \times 10^{-3}$ | $1.094 \times 10^{-2}$ |
| 0.0149 | 0.652098 | 0.643521 | $8.576 \times 10^{-3}$ | $1.315 \times 10^{-2}$ |
| 0.0177 | 0.627966 | 0.618370 | $9.596 \times 10^{-3}$ | $1.528 \times 10^{-2}$ |
| 0.0205 | 0.607399 | 0.596869 | $1.053 \times 10^{-2}$ | $1.734 \times 10^{-2}$ |
| 0.0233 | 0.589479 | 0.578089 | $1.139 \times 10^{-2}$ | $1.932 \times 10^{-2}$ |
| 0.0261 | 0.573604 | 0.561418 | $1.219 \times 10^{-2}$ | $2.124 \times 10^{-2}$ |
| 0.0289 | 0.559354 | 0.546430 | $1.292 \times 10^{-2}$ | $2.311 \times 10^{-2}$ |
| 0.0316 | 0.546427 | 0.532815 | $1.361 \times 10^{-2}$ | $2.491 \times 10^{-2}$ |
| 0.0344 | 0.534596 | 0.520345 | $1.425 \times 10^{-2}$ | $2.666 \times 10^{-2}$ |
| 0.0372 | 0.523690 | 0.508842 | $1.485 \times 10^{-2}$ | $2.835 \times 10^{-2}$ |
| 0.0400 | 0.513574 | 0.498168 | $1.541 \times 10^{-2}$ | $3.000 \times 10^{-2}$ |

Table 3: *Symmetry check for* $C(\beta)$ *for the triangular lattice around* $\beta_c = \ln 3$.

Similar to before, we can compute the modular parameter for this case by expanding $p^{\text{Tri}}$ around the

critical angles $\Theta = \Phi = 0$.

$$\begin{aligned} p^{\text{Tri}}(\theta,\phi) &= 4de\sin^2\theta + \left|p^{\text{Hex}}(e^{i\theta},e^{i\phi}) - fe^{i\theta}e^{i\phi}\right|^2 \\ &\approxeq 4de\theta^2 + \left|c - a(1-i\theta) - b(1+i\phi) - f(1+i(\theta+\phi))\right|^2 \\ &= 4de\theta^2 + \left|i(a\theta - b\phi - f(\theta+\phi))\right|^2 \\ &= (4de + (a-f)^2)\theta^2 - 2(a-f)(b+f)\theta\phi + b^2\phi^2 \end{aligned} \tag{80}$$

Now we can use the original full definitions of $\theta = \frac{2\pi(n+u)}{N}$ and $\phi = \frac{2\pi(m+v)}{M}$,

$$\begin{aligned} p^{\text{Tri}}(\theta,\phi) \approxeq \left(\frac{2\pi}{N}\right)^2 ((a-f)^2+4de)\Bigg[(n+u)^2 - \frac{2(a-f)(b+f)N}{((a-f)^2+4de)M}(n+u)(m+v) + \\ + \frac{1}{(a-f)^2+4de}\left(\frac{(b+f)N}{M}\right)^2 (m+v)^2\Bigg] \end{aligned} \tag{81}$$

This is very similar to the square-triangle case, giving the modular parameter to be:

$$\tau = \frac{(b+f)N}{M((a-f)^2+4de)}\left((a-f)^2 + 2i\sqrt{de}\right) \tag{82}$$

Eq. (82) is another key result of this work. In particular, if we set $d = 0$ or $e = 0$, the imaginary part of $\tau$ tends to zero, causing the torus geometry to collapse to a degenerate limit. This mirrors the behaviour already encountered for Eq. (57), and further emphasises the role of the $d$ and $e$ bonds in maintaining a non-degenerate modular parameter. Once the modular parameter $\tau$ has been obtained for the triangular-lattice case, the conformal field theory partition function can be written directly in terms of theta functions, exactly as in Eq. (59). This is given by the followoing:

$$\lim_{N,M\to\infty} \frac{\mathcal{Z}(N,M)}{e^{NMW(a,b,c,d,e,f)}} = \frac{1}{2}\sum_{u,v=0}^{1/2}\left|\frac{\theta[{}^{u}_{v}](0|\tau)}{\eta(\tau)}\right|^{\frac{1}{2}} \tag{83}$$

The only modification introduced by the change from the square–triangle lattice to the triangular lattice is the numerical value of $\tau$. This observation reflects an important aspect of universality: at the critical point, nearly all microscopic details of the lattice enter the continuum theory solely through $\tau$, while the functional form of the conformal partition function remains unchanged. In this way, the critical triangular-lattice dimer model lies in the same universality class, with its distinct lattice geometry encoded almost entirely in the modular parameter. It will be shown in the following section that lattices can also be distinguished by some holonomy behaviour in the lattice.

# 6 A Bipartite Hexagonal Lattice with a Defect

Now we wish to return to the original bipartite hexagonal lattice, but instead of having every bond of the same type having the same activity, we wish to study the effects of introducing a defect or rather a line of defects into the lattice. The first way we can do this is to replace the periodic $a$ bond on the lattice with some defective $\tilde{a}$ activity. This idea of introducing a duality-twisted boundary condition is talked about in a similar context in [20]. A simple $2 \times 2$ lattice example is shown in Fig. 20. Now what does the partition function look like in this case? Translations in the w direction can still be used to partly diagonalise the matrix by Fourier transforming as before, but the z direction now cannot be treated so easily due to this defect. Instead, one of the $a$ activities is replaced with an $\tilde{a}$, and the partition function reduces to the form below by computing the determinants [21].

$$\begin{aligned} \det(A\,(\tilde{a})_{u,v}) &= \prod_{m=1}^{M}(c - be^{2\pi i(m+v)/M})^N - \tilde{a}a^{N-1}e^{2\pi iu} \\ \mathcal{Z}(\tilde{a}) &= \frac{1}{2}\sum_{u,v=0}^{1/2} e^{2\pi i(1/2+u+v+2uv)}\det(A(\tilde{a})_{u,v}) \end{aligned} \tag{84}$$

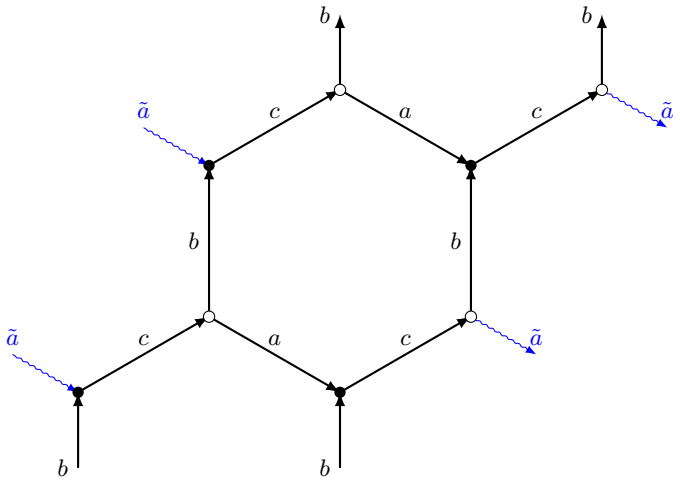



Figure 20: *Small example of our bipartite hexagonal lattice with a defect $\tilde{a}$, showing activities of the different bonds and our choice of Kasteleyn orientation.*

Different values of $\tilde{a}$ have different physical meanings For instance, $\tilde{a} = -a$ means that we now have anti-periodic boundary conditions in the horizontal direction, while $\tilde{a} = 0$ corresponds to having no periodicity in the horizontal direction. We wish to see what some of these values of $\tilde{a}$ yield for different values of bond activities $a$, $b$ and $c$. An overall result observed was that for either $N = 1$ or $M = 1$, $\mathcal{Z}(\tilde{a}) = \det(A(\tilde{a})_{\frac{1}{2},\frac{1}{2}})$.

## 6.1 Case 1: Rectangular Domain

Here, we set the values of the parameters to be such that $a^2 + b^2 = c^2$. This setup corresponds to a rectangular domain, with $\tau_0 = 0$ and $\tau_1 = \frac{Nb}{Ma}$. For this case, one of the determinants $\det(A(a)_{u,v})$ vanishes when both $M$ and $N$ satisfy the following conditions for some $n \in \mathbb{Z}_{\geq 0}$:

1. $N = 4(2n+2)$ and $M = 4(2n+2)$, which leads to $\det(A(a)_{0,0}) = 0$.
2. $N = 4(2n+2)$ and $M = 4(2n+1)$, which leads to $\det(A(a)_{0,\frac{1}{2}}) = 0$.
3. $N = 4(2n+1)$ and $M = 4(2n+2)$, which leads to $\det(A(a)_{\frac{1}{2},0}) = 0$.
4. $N = 4(2n+1)$ and $M = 4(2n+1)$, which leads to $\det(A(a)_{\frac{1}{2},\frac{1}{2}}) = 0$.

Hence, there is some form of mod 8 periodicity in this case, although this periodicity only seems to hold for these zeroes, and not for the other non-zero determinant values. Introducing a defect of the form $\tilde{a} = -a$ gave a negative valued partition function for some values of $N$ and $M$. This is due to the fact that this type of defect swaps $u = 0$ and $u = \frac{1}{2}$, as periodic and anti-periodic boundary conditions mean the opposite to what they did before. Before this, the only negative $\det(A(a)_{u,v})$ was for $u = v = 0$, which wasn't a problem since $\text{Arf}((0,0)) = -1$ in our definition, so this term was still positive. However, now this has been swapped to a $\vec{u}$ with a positive Arf invariant, and a positive term has conversely been swapped to a $\vec{u}$ with a negative Arf invariant, so the partition function can take negative values. Also, thinking about the partition function as defined in Eq. (3), this will read as:

$$\mathcal{Z} = \sum_{\text{coverings}} a^{N_a} b^{N_b} c^{N_c} \tilde{a}^{N_{\tilde{a}}} \tag{85}$$

For negative $\tilde{a}$, the partition function is no longer a sum of positive weights, and hence can take negative values.

## 6.2 Case 2: Equal weights

In this case, we consider $a = b = c$. For this case, one of the determinants $\det(A(a)_{u,v})$ vanishes when both $M$ and $N$ satisfy the following conditions for some $n \in \mathbb{Z}_{\geq 0}$:

1. $N = 3(2n+2)$ and $M = 3(2n+2)$, which leads to $\det(A(a)_{0,0}) = 0$.
2. $N = 3(2n+2)$ and $M = 3(2n+1)$, which leads to $\det(A(a)_{0,\frac{1}{2}}) = 0$.
3. $N = 3(2n+1)$ and $M = 3(2n+2)$, which leads to $\det(A(a)_{\frac{1}{2},0}) = 0$.
4. $N = 3(2n+1)$ and $M = 3(2n+1)$, which leads to $\det(A(a)_{\frac{1}{2},\frac{1}{2}}) = 0$.

Hence, there is some form of mod 6 periodicity in this case, as noted in [15]. Again, this periodicity appears to only be for these zero-valued determinants. It was also found that for $N = M$, all $\det(A(\tilde{a})_{u,v})$ with at least one twisted boundary are equal. Again, introducing a defect of the form $\tilde{a} = -a$ gave a negative valued partition function for some values of $N$ and $M$ for the same reasons as before. Introducing this defect also gives a special result for $M = 2$, where $\mathcal{Z} = a^{2N} = b^{2N} = c^{2N}$.

### 6.3 Case 3: At the edge of the Amoeba

In this case, we consider $c = a+b$, which is on the edge of the amoeba of the dimer model and corresponds to the critical point observed in Section 4. For this case, we observe that for $M = N$, the determinants of $A(a)_{u,v}$ with one twisted boundary condition are equal. We also notice that $\det(A(a)_{0,0}) = 0$ for all values of $M$ and $N$. This can lead to a special result for $M = 1$ or $N = 1$ when we introduce a second defect $\tilde{b} = -b$. In the same way that $\tilde{a} = -a$ swaps $u = 0$ and $u = \frac{1}{2}$, $\tilde{b} = -b$ swaps $v = 0$ and $v = \frac{1}{2}$. Combining this with our earlier observation that for $M = 1$ or $N = 1$, $\mathcal{Z} = \det(A(\tilde{a})_{\frac{1}{2},\frac{1}{2}})$, we get that $\mathcal{Z} = 0$ for $M = 1$ or $N = 1$ and $\tilde{a} = -a$, $\tilde{b} = -b$.

## 7 Conclusion

We have analysed a range of dimer models on bipartite and non-bipartite lattices, highlighting the deep connections between combinatorial methods, modular geometry, and conformal field theory. Our results confirm the universality of the critical behaviour across different lattice types, with differences between the non-bipartite lattices arising through modifications of the modular parameter. Numerical studies of thermodynamic observables confirm the expected critical behaviour and match analytic predictions.

An interesting direction for future work would be to probe more deeply into the results of Section 6, in particular exploring the underlying mechanism that governs the symmetry and interesting modular behaviour for the different cases. This would involve a more detailed study of the analytic structure of the partition function, similar to that done by Seiberg and Shao in [14].

# References


[1] Charles Nash and Denjoe O'Connor. Modular invariance, lattice field theories, and finite size corrections. *Annals of Physics*, 273:72–98, 1999.

[2] Richard Kenyon and Andrei Okounkov. What is ... a dimer? *Notices of the American Mathematical Society*, 52(3):342–343, 2005. PDF.

[3] P. W. Kasteleyn. Dimer statistics and phase transitions. *Journal of Mathematical Physics*, 4(2):287–293, 1963. doi: 10.1063/1.1703953.

[4] David Cimasoni and Nicolai Reshetikhin. Dimers on surface graphs and spin structures. i. *Communications in Mathematical Physics*, 275(1):187–208, July 2007. ISSN 1432-0916. doi: 10.1007/s00220-007-0302-7. URL http://dx.doi.org/10.1007/s00220-007-0302-7.

[5] Charles Nash and Denjoe O'Connor. Dimer geometry, amoebae and a vortex dimer model. *Journal of Physics A: Mathematical and Theoretical*, 50(35):355002, August 2017. ISSN 1751-8121. doi: 10.1088/1751-8121/aa8044. URL http://dx.doi.org/10.1088/1751-8121/aa8044.

[6] David Tong and Carl Turner. Notes on 8 majorana fermions. *SciPost Physics Lecture Notes*, March 2020. ISSN 2590-1990. doi: 10.21468/scipostphyslectnotes.14. URL http://dx.doi.org/10.21468/SciPostPhysLectNotes.14.

[7] Wikimedia Commons contributors. Pavage domino. https://en.wikipedia.org/wiki/File:Pavage_domino.svg, 2007. URL https://en.wikipedia.org/wiki/File:Pavage_domino.svg. Accessed: 2025-08-05.

[8] P. W. Kasteleyn. The statistics of dimers on a lattice : I. The number of dimer arrangements on a quadratic lattice. *Physica*, 27(12):1209–1225, December 1961. doi: 10.1016/0031-8914(61)90063-5.

[9] Richard Kenyon, Andrei Okounkov, and Scott Sheffield. Dimers and amoebae, 2003. URL https://arxiv.org/abs/math-ph/0311005.

[10] J Ambjørn, B Durhuus, and J F Wheater. A restricted dimer model on a two-dimensional random causal triangulation. *Journal of Physics A: Mathematical and Theoretical*, 47(36):365001, August 2014. ISSN 1751-8121. doi: 10.1088/1751-8113/47/36/365001. URL http://dx.doi.org/10.1088/1751-8113/47/36/365001.

[11] Bryce DeWitt. *Supermanifolds*. Cambridge University Press, 1984. ISBN 0-521-42377-5.

[12] D. J. Candlin. On sums over trajectories for systems with fermi statistics. *Nuovo Cimento*, 4(2):231–239, 1956. doi: 10.1007/BF02745446.

[13] R. Dijkgraaf, D. Orlando, and S. Reffert. Dimer models, free fermions and super quantum mechanics, 2007. URL https://arxiv.org/abs/0705.1645.

[14] Nathan Seiberg and Shu-Heng Shao. Majorana chain and ising model - (non-invertible) translations, anomalies, and emanant symmetries. *SciPost Physics*, 16(3), March 2024. ISSN 2542-4653. doi: 10.21468/scipostphys.16.3.064. URL http://dx.doi.org/10.21468/SciPostPhys.16.3.064.

[15] Charles Nash and Denjoe O'Connor. Topological phase transitions and holonomies in the dimer model. *Journal of Physics A: Mathematical and Theoretical*, 42(1):012002, November 2008. ISSN 1751-8121. doi: 10.1088/1751-8113/42/1/012002. URL http://dx.doi.org/10.1088/1751-8113/42/1/012002.

[16] Charles Nash and Denjoe O'Connor. Zero temperature phase diagram of the kitaev model. *Physical Review Letters*, 102(14), April 2009. ISSN 1079-7114. doi: 10.1103/physrevlett.102.147203. URL http://dx.doi.org/10.1103/PhysRevLett.102.147203.

[17] Henry Cohn, Richard Kenyon, and James Propp. A variational principle for domino tilings. *Journal of the American Mathematical Society*, 14(2):297–346, November 2000. ISSN 1088-6834. doi: 10.1090/s0894-0347-00-00355-6. URL http://dx.doi.org/10.1090/S0894-0347-00-00355-6.

[18] J. F. Nagle, Carlos S. O. Yokoi, and S. M. Bhattacharjee. Dimer models on anisotropic lattices. In C. Domb and J. L. Lebowitz, editors, *Phase Transitions and Critical Phenomena*, volume 13, pages 235–297. Academic Press, London, 1989.

[19] Andrea Pelissetto and Ettore Vicari. Critical phenomena and renormalization-group theory. *Physics Reports*, 368(6):549–727, 2002. doi: 10.1016/S0370-1573(02)00219-3.

[20] David Aasen, Roger S K Mong, and Paul Fendley. Topological defects on the lattice: I. the ising model. *Journal of Physics A: Mathematical and Theoretical*, 49(35):354001, August 2016. ISSN 1751-8121. doi: 10.1088/1751-8113/49/35/354001. URL http://dx.doi.org/10.1088/1751-8113/49/35/354001.

[21] Denjoe O'Connor and Sanjaye Ramgoolam. Gauged permutation invariant matrix quantum mechanics: Path integrals, 2024. URL https://arxiv.org/abs/2312.12397.